INDC(CCP)-0455
Distr. AD/G/IN/J/PF/RD/ST

IAEA
International Atomic Energy Agency

# INDC International Nuclear Data Committee

Translations of Selected Papers published in

Voprosy Atomhnoj Nauki i Tekniki

Series: Yadernye Konstanty (Nuclear Constants),
Issue No. 1-2, 2011-2012

Translated by IAEA

August 2014

**IAEA Nuclear Data Section**
**Vienna International Centre, P.O. Box 100, 1400 Vienna, Austria**

Selected INDC documents may be downloaded in electronic form from
*http://www-nds.iaea.org/publications*
or sent as an e-mail attachment.
Requests for hardcopy or e-mail transmittal should be directed to
*NDS.Contact-Point@iaea.org*
or to:
Nuclear Data Section
International Atomic Energy Agency
Vienna International Centre
PO Box 100
1400 Vienna
Austria

Printed by the IAEA in Austria

August 2014

**INDC(CCP)-0455**
**Distr. AD/G/IN/J/PF/RD/ST**

# Translations of Selected Papers published in

# Voprosy Atomhnoj Nauki i Tekniki

# Series: Yadernye Konstanty (Nuclear Constants), Issue No. 1-2, 2011-2012

## ABSTRACT

This report contains the translation of three papers published in the Nuclear Constants, Issue No. 1-2, 2011-2012 (Voprosy Atomnoj Nauki i Tekniki, seriya: Yadernye Konstanty (YK), vypusk 1-2, 2011-2012).

August 2014

# TABLE OF CONTENTS

**NEUTRON DATA AND PARAMETERS**

UDC 539.172

# THE BROND-3/A LIBRARY OF NEUTRON CROSS-SECTIONS FOR RESEARCH INTO THE ACTIVATION AND TRANSMUTATION OF MATERIALS*

*A.I. Blokhin, D.A. Blokhin, V.N. Manokhin, N.N. Buleeva, I.V. Sipachev*

*State Research Centre of the Russian Federation — A.I. Leipunsky Institute of Physics and Power Engineering, Obninsk*

THE BROND-3/A LIBRARY OF NEUTRON CROSS SECTIONS FOR RESEARCH INTO THE ACTIVATION AND TRANSMUTATION OF MATERIALS. This paper gives a brief description of the library of evaluated cross sections for the activation reactions *(n,2n), (n,3n), (n,p), (n,np), (n,α), (n,nα), (n,d), (n,t), (n,γ)* for 645 stable and long-lived (> 10 hours) radioactive nuclei having atomic masses in the range 1–210 (hydrogen to polonium) and in the range of neutron energies from the threshold for the given nucleus to 20 MeV. The evaluated cross sections were obtained by analysing available experimental data and theoretical excitation functions from other activation libraries using the similarity method and empirical systematics of threshold reaction excitation functions.

**Key words:** Neutron data, threshold reaction cross-sections, excitation functions, empirical systematics

## Introduction

In order to calculate the activation and transmutation of, and radiation damage to, structural and process-related materials at nuclear power facilities, specialized libraries have been set up in various countries containing evaluated threshold reaction cross-sections and radiative capture cross-sections for all stable and long-lived radionuclides with a half-life of greater than 10 hours.

For incident neutron energies up to 20 MeV, in the general case 14 threshold reactions can occur that lead to activation of the nuclides: *(n,2n), (n,3n), (n,p), (n,np), (n,α), (n,nα), (n,d), (n,t), (n,$^3$He), (n,2p), (n,nd), (n,nt), (n,n')* and radiative capture.

There are currently several relatively complete libraries of activation cross-sections: ADL-3 (Russia), JEFF-3.1.1/A (Western Europe), JENDL-3A (Japan), EAF-2010 (Western Europe).

In general, the number of nuclides included in the various libraries ranges from 500 to 800. Of these, 282 are stable and the rest are radioactive.

* Translated from Voprosy Atomnoj Nauki i Tekniki Ser. Yadernye Konstanty, No. 1-2, pp. 3-7, 2011-2012.

The evaluated data in these and other libraries were obtained by means of calculations based on theoretical models of nuclear reactions using the available experimental data to correct or refine the source data for the calculation programs.

The use of different models and input parameters in calculation programs in the absence of reliable experimental data often results in significant differences in the evaluated data from different libraries.

Extensive international cooperative efforts have been under way for many years to develop and harmonize the theoretical models, cross-section calculation programs and input parameters. One has seen a narrowing of the differences in results and a practical coincidence for a number of reactions (mainly (*n,2n*) and (*n,3n*)), although for other reactions significant discrepancies remain.

Significant efforts are being made to create and develop empirical systematics based on existing experimental data and current understanding of the mechanism of nuclear reactions. These systematics can be used to interpolate or extrapolate their predictions to cover nuclides for which there are no experimental data.

## Method of evaluation

In this paper the selection and evaluation of the data were based on the empirical systematics created at the Nuclear Data Centre for threshold reactions.

These systematics, of varying degrees of complexity, are available for incident neutron energies in the 14–15 MeV range, where most of the experimental data are concentrated. They provide useful information about the behaviour of the cross-sections of threshold reactions with a threshold below 14 MeV that can be used to verify the correctness of decisions made.

For example, for the (n,p) and (n,α) reactions they show that the cross-section varies exponentially with the atomic weight of the isotope of a given element and they give an indication of the relative values of the cross-sections for various reactions and various nuclides in a given neutron energy range.

However, this information is not sufficient to check the shape of a cross-section's energy dependence (excitation function) over the entire range of incident neutron energies from the threshold to 20 MeV.

This is why empirical systematics for excitation functions were developed at the Nuclear Data Centre for a number of years based on analysis of experimental data for the entire range of incident neutron energies, from the threshold to 20 MeV, following a systemic approach using the similarity method [1–4].

In the course of creating the library, a comparative analysis was done of all existing experimental data and the systematic tendencies in the behaviour of excitation functions arising from modelling calculations reflecting current knowledge about the mechanism of nuclear reactions. This analysis revealed a similarity in the behaviour of a number of the characteristic parameters of excitation functions — the absolute value of the cross-section at the maximum, the position of the maximum relative to the reaction threshold, the shape of the excitation function, etc. — as a function of the inherent characteristics of the nuclei: A, Z, (N-Z).

The BROND-3/A library is almost entirely built on a foundation of systematics. Each excitation function has been verified against systematics. The excitation functions for the reactions *(n,2n), (n,3n)* and *(n,d)* were calculated based on the empirical formulas. For the reactions *(n,p), (n,α), (n,np), (n,nα)* and *(n,t)* the excitation functions from other libraries were taken as a basis and

then renormalized by absolute value and corrected for shape by comparing them with the shape of neighbouring nuclei with the same Z or A.

The BROND-3/A library was created over a period of more than ten years. That process benefited from the experience gained in the creation of such libraries as ADL-3, EAF-99, EAF-2010, JEFF-3/1A, and FENDL-2/A.

## Contents of the library

The BROND-3/A library contains over 6000 excitation functions for the reactions *(n,2n), (n,3n), (n,p), (n,np), (n,α), (n,nα), (n,d), (n,t)* and radiative capture induced by neutrons at energies up to 20 MeV, for 645 nuclides.

It also includes reactions on isomeric targets and reactions yielding product nuclei in isomeric states. The table gives the full catalogue of isotopes included in the BROND-3/A library.

**Catalogue of the BROND-3/A library of neutron activation cross-sections**

| Isotope | MAT | Isotope | MAT | Isotope | MAT | Isotope | MAT |
|---|---|---|---|---|---|---|---|
| 01-H-001 | 125 | 20-CA-040 | 2025 | 29-CU-063 | 2925 | 36-KR-086 | 3649 |
| 01-H-002 | 128 | 20-CA-041 | 2028 | 29-CU-064 | 2928 | 37-RB-083 | 3719 |
| 01-H-003 | 131 | 20-CA-042 | 2031 | 29-CU-065 | 2931 | 37-RB-084 | 3722 |
| 02-HE-003 | 225 | 20-CA-043 | 2034 | 29-CU-067 | 2937 | 37-RB-085 | 3725 |
| 02-HE-004 | 228 | 20-CA-044 | 2037 | 30-ZN-064 | 3025 | 37-RB-086 | 3728 |
| 03-LI-006 | 325 | 20-CA-045 | 2040 | 30-ZN-065 | 3028 | 37-RB-087 | 3731 |
| 03-LI-007 | 328 | 20-CA-046 | 2043 | 30-ZN-066 | 3031 | 38-SR-082 | 3819 |
| 04-BE-009 | 425 | 20-CA-047 | 2046 | 30-ZN-067 | 3034 | 38-SR-083 | 3822 |
| 05-B-010 | 525 | 20-CA-048 | 2049 | 30-ZN-068 | 3037 | 38-SR-084 | 3825 |
| 05-B-011 | 528 | 21-SC-044 | 2123 | 30-ZN-069 | 3041 | 38-SR-085 | 3828 |
| 06-C-012 | 625 | 21-SC-045 | 2125 | 30-ZN-070 | 3043 | 38-SR-086 | 3831 |
| 06-C-013 | 628 | 21-SC-046 | 2128 | 30-ZN-072 | 3049 | 38-SR-087 | 3834 |
| 07-N-014 | 725 | 21-SC-047 | 2131 | 31-GA-067 | 3119 | 38-SR-088 | 3837 |
| 07-N-015 | 728 | 21-SC-048 | 2134 | 31-GA-069 | 3125 | 38-SR-089 | 3840 |
| 08-O-016 | 825 | 22-TI-044 | 2219 | 31-GA-071 | 3131 | 38-SR-090 | 3843 |
| 08-O-017 | 828 | 22-TI-046 | 2225 | 31-GA-072 | 3134 | 39-Y-086 | 3916 |
| 08-O-018 | 831 | 22-TI-047 | 2228 | 32-GE-068 | 3219 | 39-Y-087 | 3919 |
| 09-F-019 | 925 | 22-TI-048 | 2231 | 32-GE-069 | 3222 | 39-Y-088 | 3922 |
| 10-NE-020 | 1025 | 22-TI-049 | 2234 | 32-GE-070 | 3225 | 39-Y-089 | 3925 |
| 10-NE-021 | 1028 | 22-TI-050 | 2237 | 32-GE-071 | 3228 | 39-Y-090 | 3928 |
| 10-NE-022 | 1031 | 23-V-048 | 2319 | 32-GE-072 | 3231 | 39-Y-091 | 3931 |
| 11-NA-022 | 1122 | 23-V-049 | 2322 | 32-GE-073 | 3234 | 40-ZR-086 | 4013 |
| 11-NA-023 | 1125 | 23-V-050 | 2325 | 32-GE-074 | 3237 | 40-ZR-088 | 4019 |
| 11-NA-024 | 1128 | 23-V-051 | 2328 | 32-GE-076 | 3243 | 40-ZR-089 | 4022 |
| 12-MG-024 | 1225 | 24-CR-050 | 2425 | 32-GE-077 | 3246 | 40-ZR-090 | 4025 |
| 12-MG-025 | 1228 | 24-CR-051 | 2428 | 33-AS-071 | 3313 | 40-ZR-091 | 4028 |
| 12-MG-026 | 1231 | 24-CR-052 | 2431 | 33-AS-072 | 3316 | 40-ZR-092 | 4031 |
| 13-AL-026 | 1322 | 24-CR-053 | 2434 | 33-AS-073 | 3319 | 40-ZR-093 | 4034 |
| 13-AL-027 | 1325 | 24-CR-054 | 2437 | 33-AS-074 | 3322 | 40-ZR-094 | 4037 |
| 14-SI-028 | 1425 | 25-MN-052 | 2516 | 33-AS-075 | 3325 | 40-ZR-095 | 4040 |
| 14-SI-029 | 1428 | 25-MN-053 | 2519 | 33-AS-076 | 3328 | 40-ZR-096 | 4043 |
| 14-SI-030 | 1431 | 25-MN-054 | 2522 | 33-AS-077 | 3331 | 41-NB-090 | 4116 |
| 14-SI-032 | 1437 | 25-MN-055 | 2525 | 34-SE-072 | 3419 | 41-NB-091 | 4119 |
| 15-P-031 | 1525 | 26-FE-054 | 2625 | 34-SE-073 | 3422 | 41-NB-092 | 4122 |
| 15-P-032 | 1528 | 26-FE-055 | 2628 | 34-SE-074 | 3425 | 41-NB-093 | 4125 |
| 15-P-033 | 1531 | 26-FE-056 | 2631 | 34-SE-075 | 3428 | 41-NB-094 | 4128 |
| 16-S-032 | 1625 | 26-FE-057 | 2634 | 34-SE-076 | 3431 | 41-NB-095 | 4131 |
| 16-S-033 | 1628 | 26-FE-058 | 2637 | 34-SE-077 | 3434 | 41-NB-096 | 4134 |
| 16-S-034 | 1631 | 26-FE-059 | 2640 | 34-SE-078 | 3437 | 42-MO-092 | 4225 |
| 16-S-035 | 1634 | 26-FE-060 | 2643 | 34-SE-079 | 3440 | 42-MO-093 | 4228 |
| 16-S-036 | 1637 | 27-CO-056 | 2716 | 34-SE-080 | 3443 | 42-MO-094 | 4231 |
| 17-CL-035 | 1725 | 27-CO-057 | 2719 | 34-SE-082 | 3449 | 42-MO-095 | 4234 |

| Isotope | MAT | Isotope | MAT | Isotope | MAT | Isotope | MAT |
|---|---|---|---|---|---|---|---|
| 17-CL-036 | 1728 | 27-CO-058 | 2722 | 35-BR-076 | 3516 | 42-MO-096 | 4237 |
| 17-CL-037 | 1731 | 27-CO-059 | 2725 | 35-BR-077 | 3519 | 42-MO-097 | 4240 |
| 18-AR-036 | 1825 | 27-CO-060 | 2728 | 35-BR-079 | 3525 | 42-MO-098 | 4243 |
| 18-AR-037 | 1828 | 28-NI-056 | 2819 | 35-BR-081 | 3531 | 42-MO-099 | 4246 |
| 18-AR-038 | 1831 | 28-NI-057 | 2822 | 35-BR-082 | 3534 | 42-MO-100 | 4249 |
| 18-AR-039 | 1834 | 28-NI-058 | 2825 | 36-KR-078 | 3625 | 43-TC-095 | 4313 |
| 18-AR-040 | 1837 | 28-NI-059 | 2828 | 36-KR-079 | 3628 | 43-TC-096 | 4316 |
| 18-AR-042 | 1843 | 28-NI-060 | 2831 | 36-KR-080 | 3631 | 43-TC-097 | 4319 |
| 19-K-039 | 1925 | 28-NI-061 | 2834 | 36-KR-081 | 3634 | 43-TC-098 | 4322 |
| 19-K-040 | 1928 | 28-NI-062 | 2837 | 36-KR-082 | 3637 | 43-TC-099 | 4325 |
| 19-K-041 | 1931 | 28-NI-063 | 2840 | 36-KR-083 | 3640 | 44-RU-096 | 4425 |
| 19-K-042 | 1934 | 28-NI-064 | 2843 | 36-KR-084 | 3643 | 44-RU-097 | 4428 |
| 19-K-043 | 1937 | 28-NI-066 | 2849 | 36-KR-085 | 3646 | 44-RU-098 | 4431 |
| 44-RU-099 | 4434 | 50-SN-125 | 5064 | 56-BA-136 | 5643 | 63-EU-154 | 6334 |
| 44-RU-100 | 4437 | 50-SN-126 | 5067 | 56-BA-137 | 5646 | 63-EU-155 | 6337 |
| 44-RU-101 | 4440 | 51-SB-119 | 5119 | 56-BA-138 | 5649 | 63-EU-156 | 6340 |
| 44-RU-102 | 4443 | 51-SB-120 | 5123 | 56-BA-140 | 5655 | 64-GD-146 | 6407 |
| 44-RU-103 | 4446 | 51-SB-121 | 5125 | 57-LA-137 | 5722 | 64-GD-147 | 6410 |
| 44-RU-104 | 4449 | 51-SB-122 | 5128 | 57-LA-138 | 5725 | 64-GD-148 | 6413 |
| 44-RU-105 | 4452 | 51-SB-123 | 5131 | 57-LA-139 | 5728 | 64-GD-149 | 6416 |
| 44-RU-106 | 4455 | 51-SB-124 | 5134 | 57-LA-140 | 5731 | 64-GD-150 | 6419 |
| 45-RH-099 | 4513 | 51-SB-125 | 5137 | 58-CE-134 | 5819 | 64-GD-151 | 6422 |
| 45-RH-101 | 4516 | 51-SB-126 | 5140 | 58-CE-136 | 5825 | 64-GD-152 | 6425 |
| 45-RH-102 | 4522 | 51-SB-127 | 5143 | 58-CE-137 | 5828 | 64-GD-153 | 6428 |
| 45-RH-103 | 4525 | 52-TE-118 | 5219 | 58-CE-138 | 5831 | 64-GD-154 | 6431 |
| 45-RH-105 | 4531 | 52-TE-119 | 5222 | 58-CE-139 | 5834 | 64-GD-155 | 6434 |
| 46-PD-100 | 4619 | 52-TE-120 | 5225 | 58-CE-140 | 5837 | 64-GD-156 | 6437 |
| 46-PD-102 | 4625 | 52-TE-121 | 5228 | 58-CE-141 | 5840 | 64-GD-157 | 6440 |
| 46-PD-103 | 4628 | 52-TE-122 | 5231 | 58-CE-142 | 5843 | 64-GD-158 | 6443 |
| 46-PD-104 | 4631 | 52-TE-123 | 5234 | 58-CE-143 | 5846 | 64-GD-159 | 6446 |
| 46-PD-105 | 4634 | 52-TE-124 | 5237 | 58-CE-144 | 5849 | 64-GD-160 | 6449 |
| 46-PD-106 | 4637 | 52-TE-125 | 5240 | 59-PR-141 | 5925 | 65-TB-153 | 6507 |
| 46-PD-107 | 4640 | 52-TE-126 | 5243 | 59-PR-143 | 5931 | 65-TB-155 | 6513 |
| 46-PD-108 | 4643 | 52-TE-127 | 5246 | 60-ND-140 | 6019 | 65-TB-156 | 6516 |
| 46-PD-109 | 4646 | 52-TE-128 | 5249 | 60-ND-142 | 6025 | 65-TB-157 | 6519 |
| 46-PD-110 | 4649 | 52-TE-129 | 5252 | 60-ND-143 | 6028 | 65-TB-158 | 6522 |
| 47-AG-105 | 4719 | 52-TE-130 | 5255 | 60-ND-144 | 6031 | 65-TB-159 | 6525 |
| 47-AG-106 | 4723 | 52-TE-131 | 5259 | 60-ND-145 | 6034 | 65-TB-160 | 6528 |
| 47-AG-107 | 4725 | 52-TE-132 | 5261 | 60-ND-146 | 6037 | 65-TB-161 | 6531 |
| 47-AG-108 | 4729 | 53-I-124 | 5316 | 60-ND-147 | 6040 | 66-DY-154 | 6619 |
| 47-AG-109 | 4731 | 53-I-125 | 5319 | 60-ND-148 | 6043 | 66-DY-156 | 6625 |
| 47-AG-110 | 4735 | 53-I-126 | 5322 | 60-ND-150 | 6049 | 66-DY-158 | 6631 |
| 47-AG-111 | 4737 | 53-I-127 | 5325 | 61-PM-143 | 6137 | 66-DY-159 | 6634 |
| 48-CD-106 | 4825 | 53-I-129 | 5331 | 61-PM-144 | 6140 | 66-DY-160 | 6637 |
| 48-CD-108 | 4831 | 53-I-131 | 5337 | 61-PM-145 | 6143 | 66-DY-161 | 6640 |
| 48-CD-109 | 4834 | 54-XE-124 | 5425 | 61-PM-146 | 6146 | 66-DY-162 | 6643 |
| 48-CD-110 | 4837 | 54-XE-126 | 5431 | 61-PM-147 | 6149 | 66-DY-163 | 6646 |
| 48-CD-111 | 4840 | 54-XE-127 | 5434 | 61-PM-148 | 6152 | 66-DY-164 | 6649 |
| 48-CD-112 | 4843 | 54-XE-128 | 5437 | 61-PM-149 | 6155 | 66-DY-166 | 6655 |
| 48-CD-113 | 4846 | 54-XE-129 | 5440 | 61-PM-151 | 6161 | 67-HO-163 | 6719 |
| 48-CD-114 | 4849 | 54-XE-130 | 5443 | 62-SM-144 | 6225 | 67-HO-165 | 6725 |
| 48-CD-115 | 4852 | 54-XE-131 | 5446 | 62-SM-145 | 6228 | 67-HO-166 | 6728 |
| 48-CD-116 | 4855 | 54-XE-132 | 5449 | 62-SM-146 | 6231 | 68-ER-160 | 6819 |
| 49-IN-111 | 4919 | 54-XE-133 | 5452 | 62-SM-147 | 6234 | 68-ER-162 | 6825 |
| 49-IN-113 | 4925 | 54-XE-134 | 5455 | 62-SM-148 | 6237 | 68-ER-164 | 6831 |
| 49-IN-114 | 4929 | 54-XE-136 | 5461 | 62-SM-149 | 6240 | 68-ER-166 | 6837 |
| 49-IN-115 | 4931 | 55-CS-129 | 5513 | 62-SM-150 | 6243 | 68-ER-167 | 6840 |
| 50-SN-112 | 5025 | 55-CS-131 | 5519 | 62-SM-151 | 6246 | 68-ER-168 | 6843 |
| 50-SN-113 | 5028 | 55-CS-132 | 5522 | 62-SM-152 | 6249 | 68-ER-169 | 6846 |
| 50-SN-114 | 5031 | 55-CS-133 | 5525 | 62-SM-153 | 6252 | 68-ER-170 | 6849 |
| 50-SN-115 | 5034 | 55-CS-134 | 5528 | 62-SM-154 | 6255 | 68-ER-172 | 6855 |
| 50-SN-116 | 5037 | 55-CS-135 | 5531 | 63-EU-145 | 6307 | 69-TM-165 | 6913 |
| 50-SN-117 | 5040 | 55-CS-136 | 5534 | 63-EU-146 | 6310 | 69-TM-167 | 6919 |

| Isotope | MAT | Isotope | MAT | Isotope | MAT | Isotope | MAT |
|---|---|---|---|---|---|---|---|
| 50-SN-118 | 5043 | 56-BA-128 | 5619 | 63-EU-147 | 6313 | 69-TM-168 | 6922 |
| 50-SN-119 | 5046 | 56-BA-130 | 5625 | 63-EU-148 | 6316 | 69-TM-169 | 6925 |
| 50-SN-120 | 5049 | 56-BA-131 | 5628 | 63-EU-149 | 6319 | 69-TM-170 | 6928 |
| 50-SN-121 | 5052 | 56-BA-132 | 5631 | 63-EU-150 | 6322 | 69-TM-171 | 6931 |
| 50-SN-122 | 5055 | 56-BA-133 | 5634 | 63-EU-151 | 6325 | 69-TM-172 | 6934 |
| 50-SN-123 | 5058 | 56-BA-134 | 5637 | 63-EU-152 | 6328 | 70-YB-166 | 7019 |
| 50-SN-124 | 5061 | 56-BA-135 | 5640 | 63-EU-153 | 6331 | 70-YB-168 | 7025 |
| 70-YB-169 | 7028 | 73-TA-182 | 7331 | 77-IR-190 | 7722 | 81-TL-200 | 8116 |
| 70-YB-170 | 7031 | 73-TA-183 | 7334 | 77-IR-191 | 7725 | 81-TL-201 | 8119 |
| 70-YB-171 | 7034 | 74-W-178 | 7419 | 77-IR-192 | 7728 | 81-TL-202 | 8122 |
| 70-YB-172 | 7037 | 74-W-180 | 7425 | 77-IR-193 | 7731 | 81-TL-203 | 8125 |
| 70-YB-173 | 7040 | 74-W-181 | 7428 | 77-IR-194 | 7734 | 81-TL-204 | 8128 |
| 70-YB-174 | 7043 | 74-W-182 | 7431 | 78-PT-188 | 7819 | 81-TL-205 | 8131 |
| 70-YB-175 | 7046 | 74-W-183 | 7434 | 78-PT-190 | 7825 | 82-PB-200 | 8213 |
| 71-LU-169 | 7107 | 74-W-184 | 7437 | 78-PT-191 | 7828 | 82-PB-201 | 8216 |
| 71-LU-170 | 7110 | 74-W-185 | 7440 | 78-PT-192 | 7831 | 82-PB-202 | 8219 |
| 71-LU-171 | 7113 | 74-W-186 | 7443 | 78-PT-193 | 7834 | 82-PB-203 | 8222 |
| 71-LU-172 | 7116 | 74-W-187 | 7446 | 78-PT-194 | 7837 | 82-PB-204 | 8225 |
| 71-LU-173 | 7119 | 74-W-188 | 7449 | 78-PT-195 | 7840 | 82-PB-205 | 8228 |
| 71-LU-174 | 7122 | 75-RE-182 | 7516 | 78-PT-196 | 7843 | 82-PB-206 | 8231 |
| 71-LU-175 | 7125 | 75-RE-183 | 7519 | 78-PT-198 | 7849 | 82-PB-207 | 8234 |
| 71-LU-176 | 7128 | 75-RE-184 | 7522 | 79-AU-194 | 7916 | 82-PB-208 | 8237 |
| 71-LU-177 | 7131 | 75-RE-185 | 7525 | 79-AU-195 | 7919 | 82-PB-209 | 8240 |
| 72-HF-172 | 7219 | 75-RE-186 | 7528 | 79-AU-196 | 7922 | 82-PB-210 | 8243 |
| 72-HF-173 | 7222 | 75-RE-187 | 7531 | 79-AU-197 | 7925 | 83-BI-203 | 8307 |
| 72-HF-174 | 7225 | 75-RE-189 | 7537 | 79-AU-198 | 7928 | 83-BI-204 | 8310 |
| 72-HF-175 | 7228 | 76-OS-185 | 7628 | 79-AU-199 | 7931 | 83-BI-205 | 8313 |
| 72-HF-176 | 7231 | 76-OS-186 | 7631 | 80-HG-194 | 8019 | 83-BI-206 | 8316 |
| 72-HF-177 | 7234 | 76-OS-187 | 7634 | 80-HG-195 | 8022 | 83-BI-207 | 8319 |
| 72-HF-178 | 7237 | 76-OS-188 | 7637 | 80-HG-196 | 8025 | 83-BI-208 | 8322 |
| 72-HF-179 | 7240 | 76-OS-189 | 7640 | 80-HG-197 | 8028 | 83-BI-209 | 8325 |
| 72-HF-180 | 7243 | 76-OS-190 | 7643 | 80-HG-198 | 8031 | 83-BI-210 | 8328 |
| 72-HF-181 | 7246 | 76-OS-191 | 7647 | 80-HG-199 | 8034 | 84-Po-206 | 8425 |
| 72-HF-182 | 7249 | 76-OS-192 | 7649 | 80-HG-200 | 8037 | 84-Po-207 | 8428 |
| 73-TA-177 | 7316 | 76-OS-193 | 7652 | 80-HG-201 | 8040 | 84-Po-208 | 8431 |
| 73-TA-179 | 7322 | 76-OS-194 | 7655 | 80-HG-202 | 8043 | 84-Po-209 | 8434 |
| 73-TA-180 | 7325 | 77-IR-188 | 7716 | 80-HG-203 | 8046 | 84-Po-210 | 8437 |
| 73-TA-181 | 7328 | 77-IR-189 | 7719 | 80-HG-204 | 8049 | | |

## References


1. A.I. Blokhin, V.N. Manokhin, S.M. Nasyrova. Izuchenie funktsij vozbuzhdeniya porogovykh reaktstij metodom podobiya (Study of excitation functions for threshold reactions using the method of similarity): Preprint FEI-2620, Obninsk, 1997.
2. V.N. Manokhin, A.I. Blokhin. Empirical dependence of parameters of neutron threshold reaction excitation functions on A, Z, (N-Z), Proc. Int. Conf. on Nuclear Data for Science and Technology, Trieste, Italy, 1997.
3. A.I. Blokhin, V.N. Manokhin, B.I. Fursov, A.N. Andrianov, V.M. Chernov. Obespechenie issledovanij aktivatsionnykh i transmutatsionnykh kharakteristik konstruktsionnykh materialov yaderno-fizicheskimi dannymi (Supporting studies of the activation and transmutation characteristics of structural materials with nuclear physics data) // Voprosy atomnoj nauki i tekhniki, ser. Yadernye konstanty, 2005, No. 1–2, p. 56.
4. A.I Blokhin, D.A. Blokhin, V.N. Manokhin, I.V. Sipachev. Otsenka sechenij porogovykh reaktsij dlya biblioteki aktivatsionnykh dannykh BROND-3/A (Evaluation of cross-sections for threshold reactions for the BROND-3/A activation data library): Preprint FEI-3226, Obninsk, 2012.

UDC 621.039

# PECULIARITIES OF THE *D+T* NEUTRON SPECTRUM FOR THICK TARGETS*

*V. S. Shorin*

*State Scientific Centre — A.I. Leipunsky Institute of Physics and Power Engineering, Obninsk*

PECULIARITIES OF THE *D+T* NEUTRON SPECTRUM FOR THICK TARGETS. The energy and angular distributions of neutrons emitted from a thick target in the reaction $^{3}$H(*d,n*)$^{4}$He were calculated using the Monte Carlo method based on the SRIM code. The first moments of the spectrum, namely mean neutron energy, energy spread and neutron yield, were determined at deuteron energies below 500 keV. The effect of the composition of the tritium target on the neutron spectrum was determined. The results obtained were compared with the available data.

## Introduction

Monoenergetic neutron sources based on the reaction $^{3}$H(*d,n*)$^{4}$He are widely used in scientific and applied research [1]. For this reason, knowledge of the distribution function $F(E_n, \theta)$ for the energy $E_n$ and angle θ of the emitted neutrons and of its dependency on incident deuteron energy is very important [2]. This function also depends on the thickness and composition of the target and the structural material surrounding it. A number of computer programs have been developed to model deuteron transport in the target and neutron production and propagation in the surrounding medium to the sample under study or the neutron detector [3]. These programs [4, 5] use a diffusion model of ion slowing in which multiple scattering is calculated in small-angle approximation.

In the simplest model of slowing down, which ignores the fluctuation in ionization losses and the multiple scattering of ions, when the trajectory of the slowing ion is linear the emitted neutron spectrum $F(E_n, \theta)$ has the form

$$F(E_n,\mu) = \varphi(\varepsilon,\mu)[d\varepsilon_n(\varepsilon,\mu)/d\varepsilon,]^{-1}, \quad (1)$$

where $\varphi(\varepsilon,\mu) = \text{const}[d\sigma_{dn}/d\Omega(\varepsilon,\mu)]S(\varepsilon)^{-1}$.

Here, $\mu = \cos\theta$; $\varepsilon(x)$ is the mean deuteron energy at target depth $x$; $E_n = \varepsilon_n(\varepsilon,\mu)$ is a kinematic function of deuteron energy and neutron exit angle; $d\sigma_{dn}/d\Omega(\varepsilon,\mu)$ is the differential cross-section for the (*d,n*) reaction; and $S(\varepsilon) = d\varepsilon/dx$ is the stopping power of the target material.

For thick targets, where deuteron trajectories in the target have a complex shape owing to multiple scattering, this approach can lead to wrong conclusions.

* Translated from Voprosy Atomnoj Nauki i Tekniki Ser. Yadernye Konstanty, No. 1-2, pp. 27-36, 2011-2012.

In this paper, to model the spectra of neutrons emitted from thick targets a stochastic model of slowing based on the Monte Carlo method is used. Neutron scattering by structures is not considered.

## 1. Calculation procedure

Deuteron trajectories in a tritium target were calculated using the SRIM program (version 2011.06) [6]. A picture of deuteron distribution by depth in a thick $TiT_2$ target for deuterons at normal incidence (total number $N_d = 10^4$ particles) with initial energies 50 and 350 keV is shown in Fig. 1. It can be seen that as deuteron energy decreases, the effects of multiple scattering increase, and the divergence of the beam increases rapidly. For the case of $E_d$ = 350 keV, the mean path of the deuterons is 5.0 μm and its radial component is 0.6 μm; for $E_d$ = 50 keV these are 1.0 and 0.31 μm, respectively. As the energy decreases, the proportion of back-scattered particles increases sharply: at $E_d$ = 350 keV it is 0.01% and at $E_d$ = 50 keV it is 0.35%.

In the SRIM program, the ion trajectory (EXYZ output file) is a piecewise linear function of the coordinates (*x, y, z*) and the deuteron energy $E_l$ giving the points on the trajectory. The mean number of trajectory nodes *m* is 30 for $E_d$ = 50 keV and 46 for $E_d$ = 350 keV.

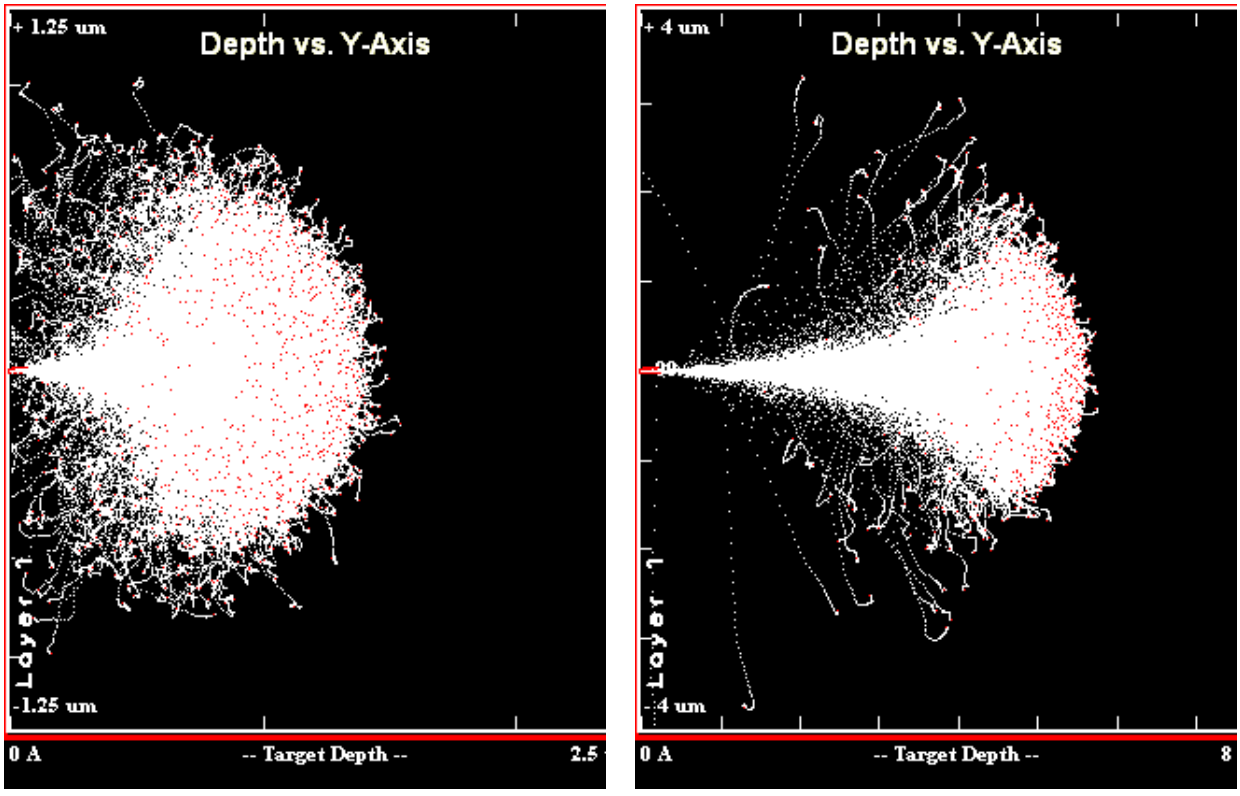


Fig. 1. Deuteron trajectories in a thick $TiT_2$ target for deuterons at normal incidence (total number $N_d = 10^4$ particles) with initial energies of 50 keV (left) and 350 keV (right)

The spectrum $F(E_n, \overline{\theta}_n)$ of neutrons exiting at an average angle of $\overline{\theta}_n$ to the original direction of the deuteron beam toward the sample in solid angle $\Omega_s$ was calculated by integrating the trajectory of deuterons slowing down in the target using the relation

$$F(E\mathrm{n}, \overline{\theta}\mathrm{n}) = \mathrm{const} \cdot C0 = \sum_{i=1}^{N_d} \sum_{k=0}^{m-1} \int_0^{l_k} dl \int_{\Omega_s} d\Omega_n \left[ d\sigma_{dn}/d\Omega \quad (E_n, \mu) \right]. \qquad (2)$$

Here, $C_0$ is the concentration of tritium in the target; $l_k$ is the length of the trajectory between nodes ($k$, $k$+1): $l_k = \left[\Delta x_k^2 + \Delta y_k^2 + \Delta z_k^2\right]^{1/2}$, $\Delta x_k = x_{k+1} - x_k$ etc., and ($x_k$, $y_k$, $z_k$) are the coordinates of the $k$-th node; $l$ is the length of the segment of the trajectory to the $k$-th node. The direction of the ion in section ($k$, $k$+1) is given by the directional cosines $\Omega_x = \Delta x_k/l_k$, $\Omega_y = \Delta y_k/l_k$, $\Omega_z = \Delta z_k/l_k$. The direction of the exiting neutron is given by the vector $\mathbf{\Omega}_n$ and the neutron's exit angle θ in relation to the direction of the ion ($\mu = \mathbf{\Omega}\cdot\mathbf{\Omega}_n$). The reaction cross-section $d\sigma_{dn}/d\Omega(E_l, \mu)$ is calculated for deuteron energy $E_l = E_k + [(E_{k+1} - E_k)/l_k](l - l_k)$, where $E_k$ is the ion's energy for the $k$-th node. The neutron's energy after exiting, $E_n$, is calculated using the function $\varepsilon_n(E_l, \mu)$.

The neutron spectrum was calculated on the surface of a sample with a radius of 2 cm at a distance of $h$ = 80 cm from the target, i.e. in a solid angle of 1.963 msr. The width of the energy channel is 40 keV. This study focused on normal incidence of a broad deuteron beam homogeneously distributed in a circle of radius $R_d$ = 4 mm on the surface of the target. Integration over the surface of the target and sample was done by the Monte Carlo method.

The function $\varepsilon_n(E_l, \mu)$ was calculated using the relativistic kinematic formula for two-particle nuclear reactions and the *Audi-93* atomic mass tables [7]. Data for the cross-section $d\sigma_{dn}/d\Omega$ in the centre-of-mass system were taken from [8] (DROSG-2000).

## 2. Calculation results

Fig. 2 shows the calculated spectra $F(E_n, \theta_n)$ of neutrons exiting a thick $TiT_2$ target for initial deuteron energy 250 keV and various emission angles $\theta_n$. The spectrum appears at first glance to be symmetrical with respect to $\theta_n$ = 90°, where its width is narrowest. However, its width differs noticeably between the forward and backward angles, it being 580 keV at 15° and 400 keV for $\theta_n$ = 165°. Multiple scattering of the deuterons results in a plateau in the spectrum (at the 0.1% level) in the high-energy part of the spectrum for backward angles and in the low-energy part for forward angles — this is noticeably less than the mean width for $\theta_n$ = 0°.

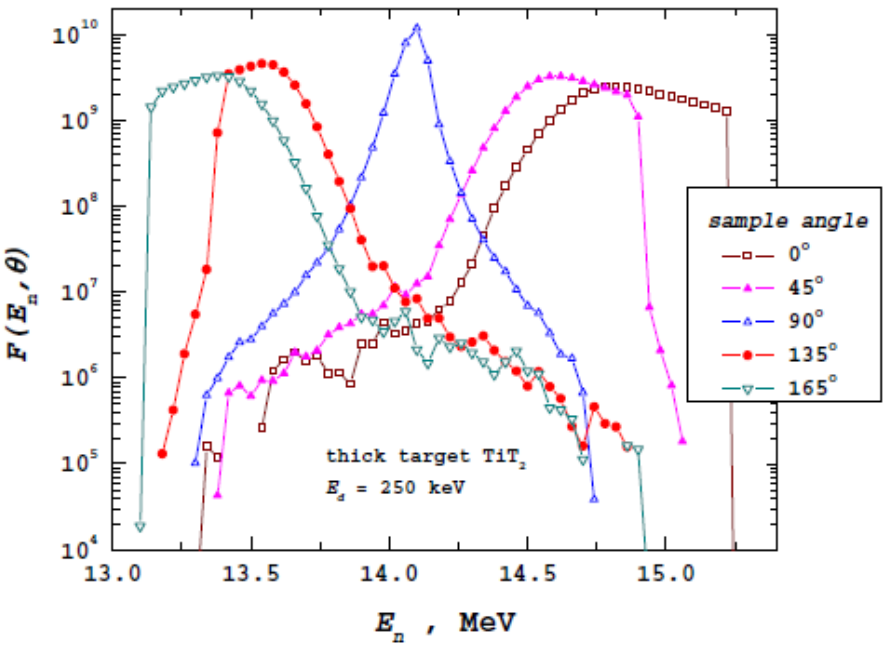


Fig. 2. Neutron spectra $F(E_n, \theta_n)$ from a $TiT_2$ target for initial deuteron energy 250 keV and various emission angles $\theta_n$.

Fig. 3 shows the shape of the spectra $F(E_n, \theta_n)$ at $\theta_n = 0°$ as a function of incident deuteron energy in the $E_d$ = 50–350 keV range. The shape of the high-energy part of the spectrum is described well by the simple model (1), as seen in Fig. 4, which shows the results of calculations for $E_d$ = 350 keV. The difference in the low-energy part is due to the effects of multiple scattering of deuterons. These effects are visible in the spectrum for a thin target (0.333 mg/cm$^2$), where, except in the main part of the spectrum, there appears a plateau whose level rises with increasing target thickness.

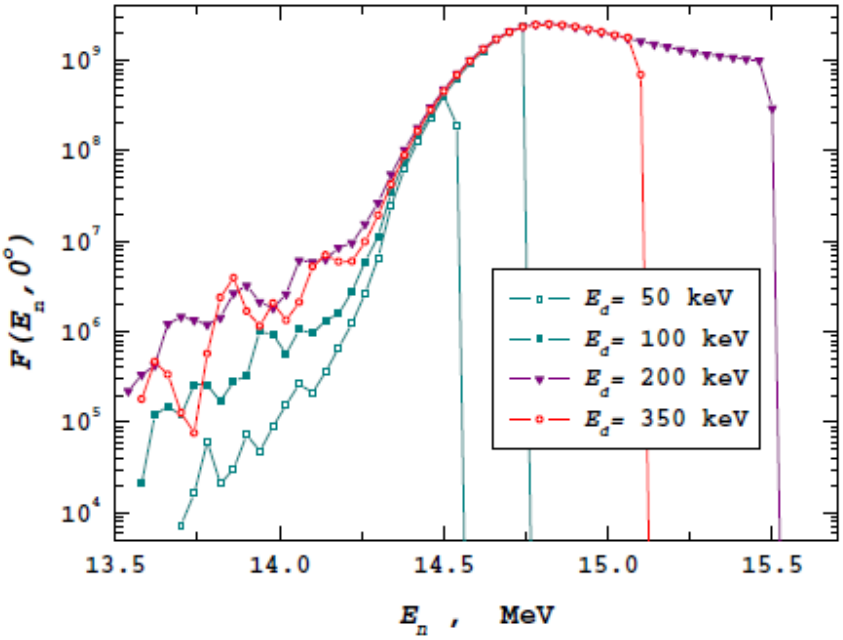


Fig. 3. Neutron spectra $F(E_n, \theta_n)$ for $\theta_n = 0°$ and initial deuteron energy $E_d$ = 50–350 keV.

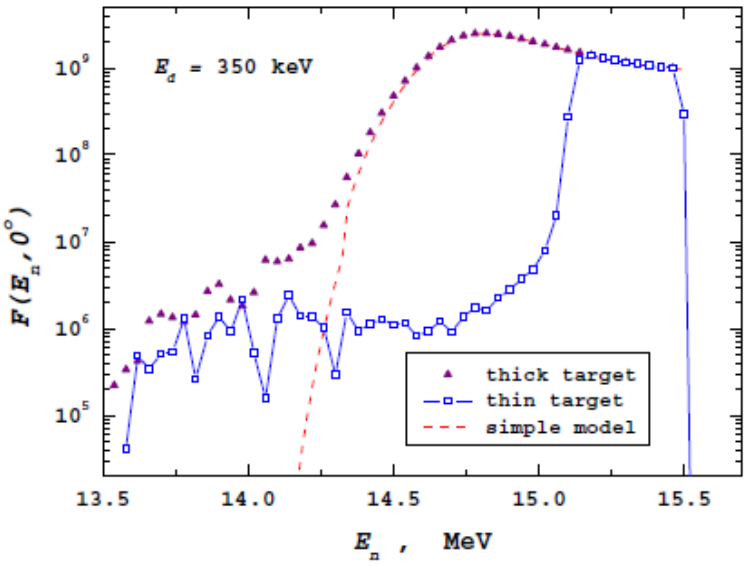


Fig. 4. Neutron spectra $F(E_n, \theta_n)$ for a thick (▲) and thin (□) $TiT_2$ target at initial deuteron energy 350 keV and exit angle 0°. The dashed line represents calculations under model (1).

The effect of multiple scattering on the shape of the main part of the neutron spectrum for emission angle 0° is shown in Fig. 5. A comparison of the spectra $F(E_n, \theta_n)$ at initial deuteron energies of 350 and 500 keV with calculations under the simple model (1) revealed a 6% discrepancy in the vicinity of the spectrum's maximum. As the deuteron energy increases, so does the number of events in the low-energy part of the spectrum (the left tail of the distribution).

For $\theta_n = 90°$ (Fig. 6), the shape of the spectrum is a peak whose width is noticeably less than the average width for 0°. Mean neutron energy $\overline{E}_n$ varies slightly as initial deuteron energy increases (see Table 1). In the $E_d = 50–350$ keV range, the mean energy change is 44 keV, while for $\theta_n = 0°$ it is 477 keV.

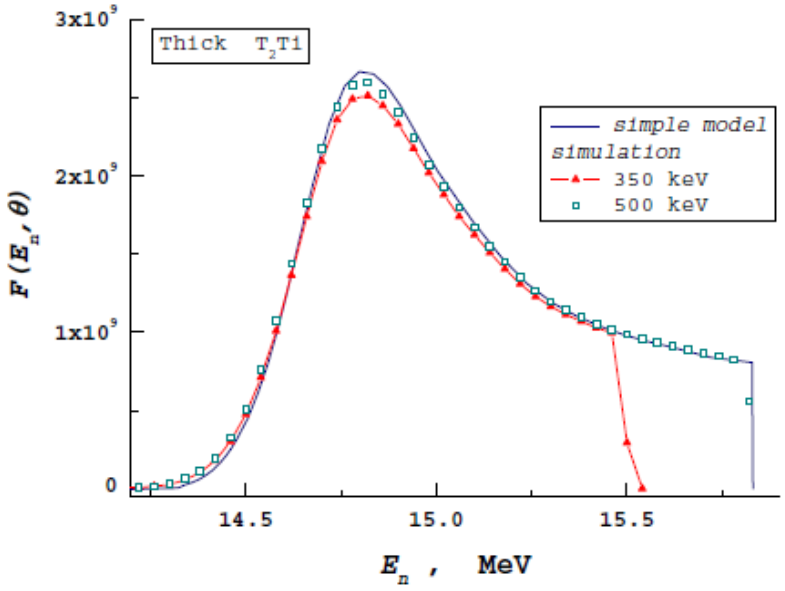


Fig. 5. Neutron spectra $F(E_n, \theta_n)$ at exit angle 0° for a thick $TiT_2$ target. Initial deuteron energy is 350 keV (▲) and 500 keV (□). The solid line represents calculations under model (1).

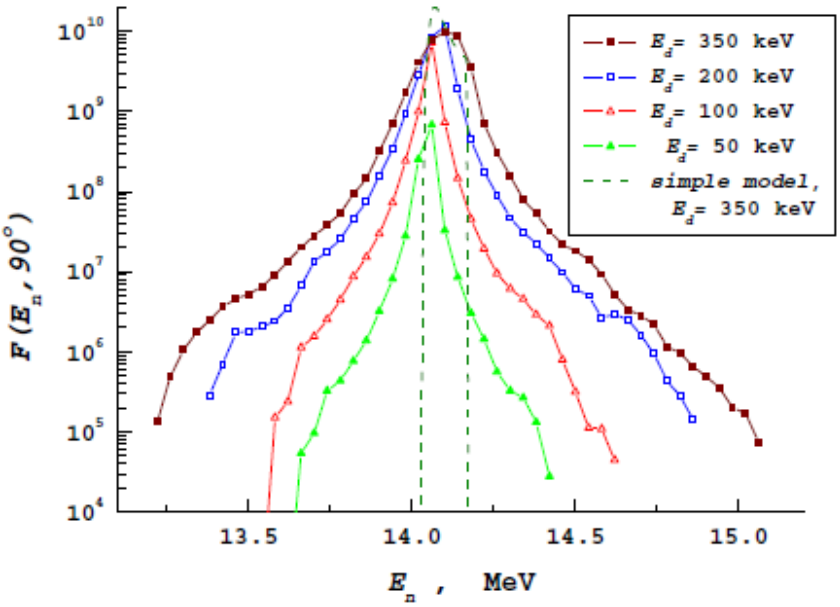


Fig. 6. Neutron spectra $F(E_n, \theta_n)$ from a thick $TiT_2$ target at exit angle 90° in the deuteron energy range $E_d$ = 50–350 keV. The dashed line represents calculations under model (1).

Table 1.

**Parameters of the angular dependency of average neutron energy $\overline{E}_n$ (μ) as a function of initial deuteron energy**

| $E_d$ (keV) | Reference | $\overline{E}_n(0)$ | $\alpha_1$ | $\beta_1$ | $\overline{E}_n(1)$ |
|---|---|---|---|---|---|
| | | MeV | | | |
| 50 | [2] | 14.06520 | 0.42329 | 0.00682 | 14.495 |
| | * | 14.0485 | 0.41274 | 0.01302 | 14.474 |
| 100 | [2] | 14.07883 | 0.57613 | 0.01222 | 14.667 |
| | * | 14.0572 | 0.57958 | 0.01102 | 14.648 |
| 150 | [2] | 14.06942 | 0.66776 | 0.01600 | 14.753 |
| | * | 14.0684 | 0.66628 | 0.0171 | 14.752 |
| 200 | [2] | 14.09680 | 0.72427 | 0.01908 | 14.840 |
| | * | 14.0765 | 0.72045 | 0.02181 | 14.8187 |
| 250 | [2] | 14.10286 | 0.76661 | 0.02167 | 14.891 |
| | * | 14.0824 | 0.7633 | 0.02434 | 14.870 |
| | ** | 14.0825 | 0.76402 | 0.02339 | 14.870 |
| 300 | [2] | 14.10803 | 0.80001 | 0.02374 | 14.932 |
| | * | 14.088 | 0.79745 | 0.02738 | 14.9128 |
| 325 | [2] | 14.10723 | 0.79477 | 0.02347 | 14.9255 |
| 350 | * | 14.0928 | 0.82762 | 0.03081 | 14.9512 |
| 500 | * | 14.107 | – | – | 15.0545 |

* results of calculations using formula (2) for the forward hemisphere of emission angles;
** results of calculations using formula (2) for all emission angles.

The increase in the root-mean-square spread $\sigma_E$ of neutron energy (see Table 2) with increasing energy $E_d$ is 43.4 keV for $\theta_n = 90°$ and 204 keV for $\theta_n = 0°$. The average width of the spectrum $\Delta_E = 2.355\sigma_E$ for 90° in the simple model (1) is 0.396 $E_d$. The mean spread is given in the last column of Table 2. A comparison with the results of modelling shows that the contribution of multiple scattering of deuterons increases at low energies.

Table 2.

**Angular parameters (keV) of mean neutron energy spread $\sigma_E$ (μ) as a function of initial deuteron energy $E_d$. Results of calculations under models (1) and (2)**

| $E_d$ (keV) | μ | $\sigma_E(1)$ (2) | $\alpha_3$ | $\beta_3$ | $\gamma_3$ | $\sigma_E(0)$ (2) | $\sigma_E(0)$ (1) |
|---|---|---|---|---|---|---|---|
| 50 | $\geq 0$ | 56.8 | 7.31 | 13.41 | | 35.05 | 8.076 |
| 100 | $\geq 0$ | 90.3 | 21.35 | 49.77 | -17.9 | 37.72 | 16.48 |
| 150 | $\geq 0$ | 127.5 | 29.43 | 74.57 | -25.35 | 48.77 | 24.90 |
| 200 | $\geq 0$ | 163.6 | 45.71 | 87.2 | -28.05 | 58.64 | 33.30 |
| 250 | $\geq 0$ | 197.2 | 65.24 | 109.2 | -41.96 | 64.66 | 41.71 |
| 250 | $\geq 0$ | 139.2 | 60.92 | 229.48 | 93.955 | 64.61 | |
| 300 | $\geq 0$ | 228.8 | 79.96 | 116.8 | -41.1 | 73.02 | 50.11 |
| 350 | $\geq 0$ | 260.4 | 101.2 | 129.28 | -48.68 | 78.44 | 58.51 |
| 500 | $\geq 0$ | 350.7 | – | – | – | 93.7 | 84.25 |

Reference [2] gives an evaluation of the average energy $\overline{E}_n(\mu)$ and of the normalized neutron yield $R = Y(\mu)/Y(0)$ for thick $TiT_2$ targets. It was demonstrated that their dependency on the emission angle in the laboratory system of coordinates can be described using the relation

$$\varphi_k(\mu) = \varphi_k(0) + \mu(\alpha_k + \mu(\beta_k + \gamma_k\mu)), \quad (3)$$

where $\varphi_1 = \overline{E}_n$, $\varphi_2 = R$, $R(0) = 1$.

The modelling results confirm these conclusions. Figs 7–9 show the angular dependencies in the $-1 \le \mu \le 1$ range for the average energy $\overline{E}_n(\mu)$, the relative neutron yield $R(\mu)$ and the root-mean-square deviation of neutron energy $\sigma_E(\mu)$ at a deuteron energy of 250 keV. For the remaining deuteron energies, the parameters $\varphi_k(0)$, $\alpha_k$, $\beta_k$, $\gamma_k$ for approximating mean energy, relative yield and average deviation $\sigma_E(\mu) = \varphi_3(\mu)$ (see Tables 1–3) were obtained only for the forward hemisphere of the exit angles.

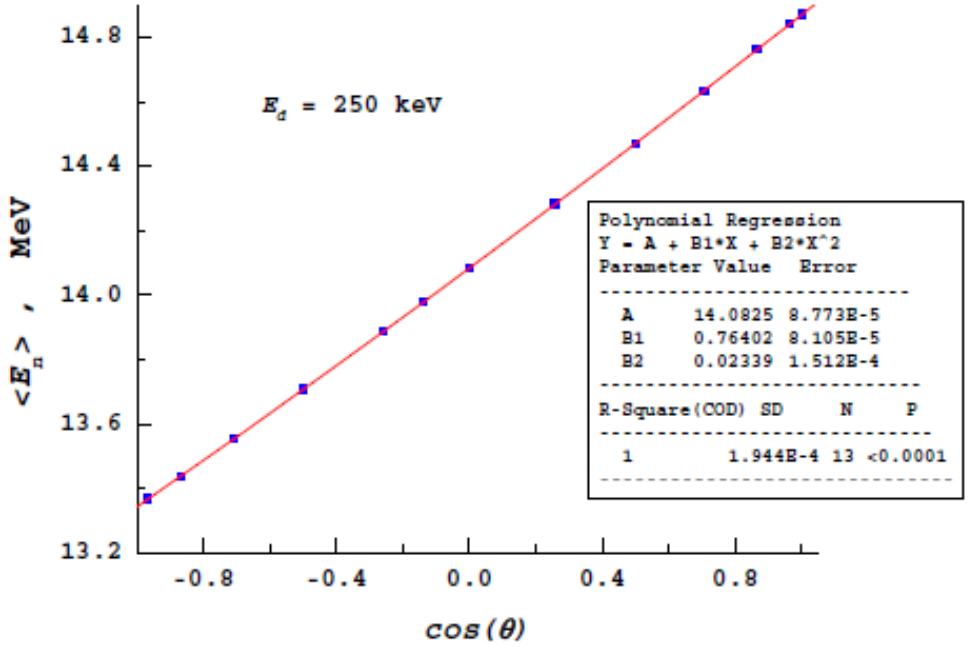


Fig. 7. Mean energy $< E_n >$ as a function of angle θ and its approximation for $E_d$ = 250 keV. The parameters for the fitting function are shown in the insert.

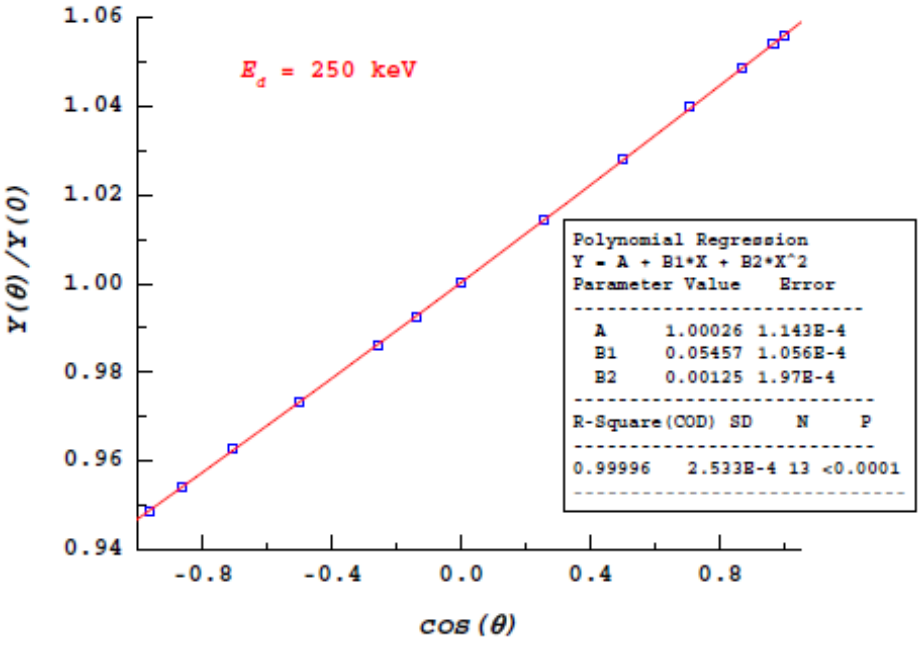


Fig. 8. Relative neutron yield $R = Y(\theta) / Y(0)$ as a function of angle θ and its approximation for $E_d$ = 250 keV. The parameters for the fitting function are shown in the insert.

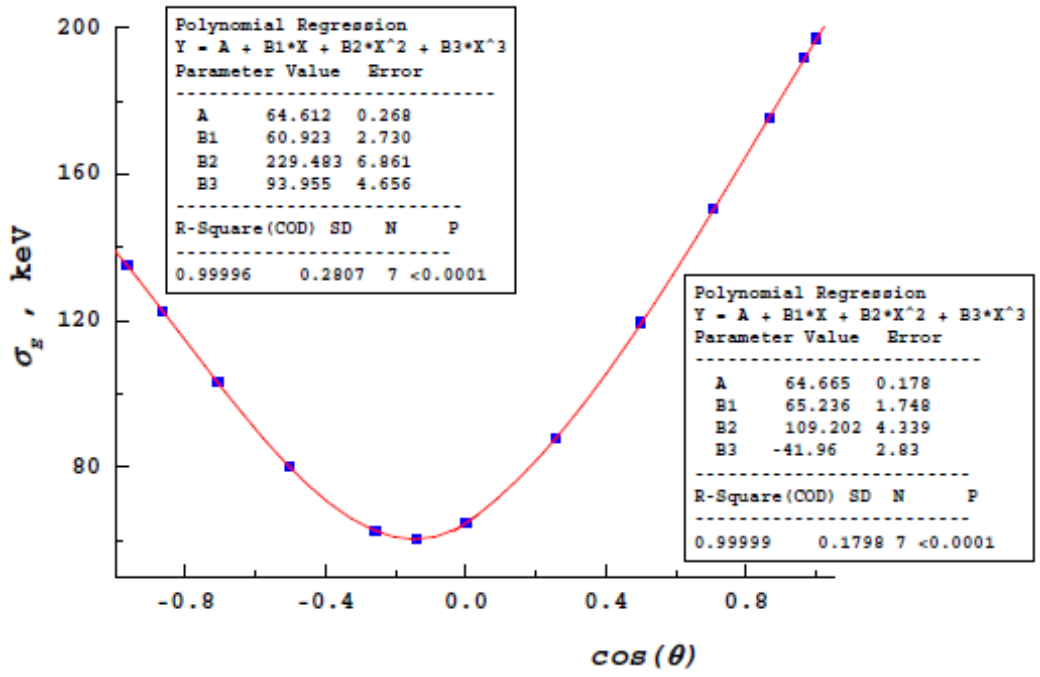


Fig. 9. Root-mean-square deviation of neutron energy σ(θ) as a function of angle θ and its approximation for $E_d$ = 250 keV. The parameters for the approximation function are given in the insert on the left for back and on the right for front neutron exit angles.

Table 3.

**Angular parameters of the neutron yield ratio as a function of initial deuteron energy (R(0) = 1)**

| $E_d$ (keV) | Reference | $R(1)$ | $\alpha_2$ | $\beta_2$ | $\gamma_2$ | $Y(1)$ 1/(μC·sr) |
|---|---|---|---|---|---|---|
| 50 | [2] | 1.0304 | 0.03003 | 0.00035 | | |
| | * | 1.0307 | 0.02963 | 0.00639 | -0.00534 | 5.3544 E5 |
| 100 | [2] | 1.0415 | 0.04087 | 0.00062 | | |
| | * | 1.042 | 0.04361 | -0.0014 | | 5.0392E6 |
| 150 | [2] | 1.0481 | 0.04727 | 0.00083 | | |
| | * | 1.04852 | 0.04688 | 0.00718 | -0.00553 | 1.0725E7 |
| 200 | [2] | 1.0512 | 0.05124 | 0.00096 | | |
| | * | 1.0471 | 0.05082 | 0.00742 | -0.00558 | 1.4569E7 |
| 250 | [2] | 1.0553 | 0.05419 | 0.00110 | | |
| | * | 1.05577 | 0.0538 | 0.00755 | -0.00556 | 1.7212E7 |
| | ** | 1.0561 | 0.05457 | 0.00125 | | |
| 300 | [2] | 1.0577 | 0.5651 | 0.00119 | | |
| | * | 1.05832 | 0.0562 | 0.00771 | -0.00559 | 1.9179E7 |
| 350 | * | 1.06059 | 0.05834 | 0.00778 | -0.00553 | 2.0788E7 |
| 500 | * | 1.0663 | – | – | – | 2.533E7 |

* results of calculations using formula (2) for the forward hemisphere of emission angles;
** results of calculations using formula (2) for all emission angles

Calculations using formula (2) generally confirm the evaluation of the values for $\overline{E}_n(\mu)$ in [2], although they also show values for $\overline{E}_n(1)$ and $\overline{E}_n(0)$ that are approx. 20 keV lower (see Table 1). The $\alpha_1$ parameters coincide to within less than 1%.

In [2], the dependency of the mean energy < $E_n$ > on the angle θ was verified experimentally at energies of 125 and 150 keV by measuring the ratio of the activities of the nuclei produced in the following (*n*,2*n*) reactions: $^{89}$Zr/$^{92m}$Nb, $^{89}$Zr/$^{180m}$Ta and $^{89}$Zr/$^{196}$Au. The measurements were compared

with the calculations of A. Pavlik and G. Winkler based on relativistic kinematics (see Table 4). The root-mean-square deviation of the experimental data from the calculated data at 150 keV is 20 keV for $\overline{E}_n(0)$ and 14 keV for $\overline{E}_n(1)$; at 125 keV it is 18.5 and 9.2 keV respectively. The results of the calculations using formula (2) were 16 and 16.7 keV for the former, 17.7 and 9.1 keV for the latter. From this it follows that the results of our work do not contradict the experimental data, since the error in the latter is almost certainly no better than 20 keV.

Table 4.

**Calculated and experimental parameters for the angular dependency of average neutron energy $\overline{E}_n(\mu)$ for $E_d$ = 150 keV**

| Method | | $\overline{E}_n(0)$ | $\alpha_1$ | $\beta_1$ | $\overline{E}_n(1)$ |
|---|---|---|---|---|---|
| $E_d$ = 150 keV | | | | | |
| Calculation | [2] | 14.0645 | 0.653 | 0.016 | 14.7335 |
| | (2) | 14.0684 | 0.66628 | 0.0171 | 14.752 |
| Measurements [2] | Nb/Zr | 14.0862 | 0.658 | 0.010 | 14.7542 |
| | Ta/Zr | 14.0820 | 0.644 | -0.001 | 14.725 |
| | Au/Zr | 14.0846 | 0.649 | 0.008 | 14.742 |
| $E_d$ = 125 keV | | | | | |
| Calculation | [2] | 14.0617 | 0.6283 | 0.0149 | 14.7049 |
| | (2) | 14.0628 | 0.6229 | 0.0141 | 14.700 |
| Measurements [2] | Nb/Zr | 14.0602 | 0.6046 | 0.0469 | 14.7117 |
| | Ta/Zr | 14.0894 | 0.5984 | 0.0166 | 14.7044 |
| | Au/Zr | 14.0777 | 0.5963 | 0.0192 | 14.6905 |

In [2] note is made of the need to investigate the function for the root-mean-square spread of neutron energy, $\sigma(E_d, \theta)$. Unlike the behaviour of the functions $\overline{E}_n(\mu)$ and $R(\mu)$ (see Figs 7–8) the angular dependency of the function $\sigma_E(\mu)$ shows some symmetry with respect to $\mu = \mu_{min}$, with $\mu_{min} = -0.1458$ for $E_d$ = 250 keV or $\theta$ = 98.4°, as can be seen in Fig. 9. In this paper, it was described using function (3), whose parameters were different for back and front neutron exit angles. For the remaining deuteron energies, Table 2 gives approximation parameters for $\mu \geq 0$ only.

Calculations by A. Pavlik and G. Winkler [2] of the width of spectrum $\Delta_E(\theta)$ for $E_d$ = 150 keV give values of $\Delta_E(0°)$ = 286 keV and $\Delta_E(90°)$ = 126 keV; in this paper they are 300 and 115 keV, respectively. For $E_d$ = 125 keV the value obtained in [2] was $\Delta_E(90°)$ = 72 keV; in this paper it is 102 keV; i.e., as energy decreases, the role of multiple scattering of incident deuterons increases.

Table 3 gives the angular parameters for describing the relative neutron yield $R(\mu)$ and the absolute value of the differential yield at $\theta_n$ = 0°. A comparison with the results in [3] shows good agreement of values for $R(E_d,1)$; the greatest discrepancy, 0.4%, is observed at $E_d$ = 200 keV.

Fig. 10 shows the effect of the chemical composition of thick tritium targets on the neutron spectra for a deuteron energy of 50 keV and $\theta_n$ = 0° and 90°. Targets composed of $TiT_x$ ($x$ = 2 and $x$ = 1.5) and $T_2O$ were investigated. For spectra at $\theta_n$ = 0° noticeable differences appear in the low neutron energy range. The presence of heavier nuclei in the target has a weak effect on the average energy $\overline{E}_n(\mu)$, as seen in Table 5. However, the mean energy spread $\sigma_E(\mu)$ is sensitive to their presence. As the effective nuclear charge decreases, the variance $\sigma_E(0)$ decreases from 36.6 keV ($TiT_{1.5}$) to 26.5 keV ($T_2O$), and $\sigma_E(1)$ decreases from 57.7 keV to 52.2 keV, respectively. We note that the variance for 90°, which is due to the kinematics of the reaction, is equal to 8.1 keV. The observed effects can be explained by the increasing role of nuclear slowing down of the deuterons at low energies as the electric charge of the target nucleus increases.

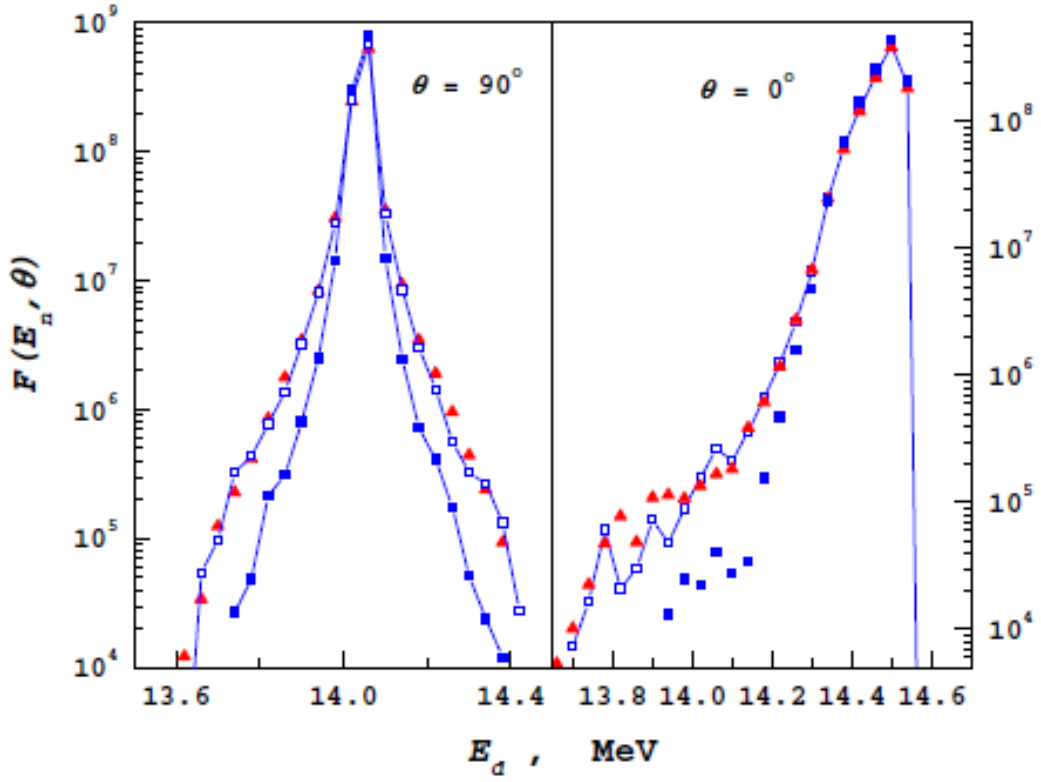


Fig. 10. Neutron spectra $F(E_n, \theta_n)$ for initial deuteron energy 50 keV and $\theta_n$ = 0° and 90° for thick targets composed of $TiT_2$ (□), $TiT_{1.5}$ (▲) and $T_2O$ (■).

Table 5.

**Effect of tritium target composition on the first moments of the neutron spectrum $\overline{E}_n(\mu)$ and $\sigma_E(\mu)$ for $\theta_n$ = 0° and 90° at $E_d$ = 50 keV**

| Target | $\overline{E}_n(1)$ | $\overline{E}_n(0)$ | $\sigma_E(1)$ | $\sigma_E(0)$ |
|---|---|---|---|---|
| | MeV | | keV | |
| $TiT_{1.5}$ | 14.4746 | 14.0483 | 57.7 | 36.6 |
| $TiT_2$ | 14.474 | 14.0485 | 56.8 | 35.05 |
| $T_2O$ | 14.4765 | 14.0485 | 52.2 | 26.5 |

In conclusion, we note that the calculations performed, which accurately take into account the trajectory of the decelerating deuterons in the target, confirmed existing estimates of the average energy and yield of neutrons from thick targets. They helped to refine substantially the estimate of the root-mean-square deviation in the energy and obtain the angular dependency parameters. The dependency of these parameters on target composition confirms the importance of choosing the correct model of the slowing down of deuterons in a thick target. The results obtained make it possible to evaluate the errors in calculations performed using computer programs employing simpler models.

The author is grateful to S.P. Simakov for his useful advice and valuable comments.

## References


1. Vlasov, N.A., Nejtrony [Neutrons]. Moscow: Nauka, GRFML, 1971. 2nd edition, chapter 2.
2. J. Csikai, Zs. Lantos, and Cs.M. Buczkö. In: Properties of Neutron Sources. IAEA-TECDOC-410, IAEA, Vienna, 1987, pp 296–301.
3. S.P. Simakov and F. Käppeler. Neutron Sources Spectra for EXFOR. INDC(NDS)-0590, IAEA, Vienna, 2011, p.55.
4. V.M. Piksaikin, V.S. Shorin, and R.G. Tertytchnyi. Fission Rate Determination in Delayed Neutron Emission Measurements with T(p,n) and D(d,n) Neutrons. INDC(CCP)-422, IAEA, Vienna, 1999.
5. A. Milocco and A. Trkov. Modelling of the Production of Source Neutrons from Low-Voltage Accelerated Deuterons on Titanium-Tritium Targets. Science and Technology of Nuclear Installations (Hindawi Publ. Corp.), v. 2008, Article ID 340282, pp 1–7.
6. J.F. Ziegler, M.D. Ziegler and J.P. Biersack. *SRIM—The Stopping and Range of Ions in Solids*. Nucl. Instr. and Meth., B268, 1818–1823 (2010).
7. G. Audi and A.H. Wapstra. “The 1993 Atomic mass evaluation”, Nucl. Phys., **A565**, 1993, p.1.
8. M. Drosg and O. Schwerer. In: Handbook on Nuclear Activation Data. Tech. rep. 273, IAEA, Vienna, 1987, p.83.

UDC 539.17

# INTEGRAL PROMPT NEUTRON SPECTRUM FOR FISSION OF $^{235}$U BY THERMAL NEUTRONS*

*A.S. Vorobyev, O.A. Shcherbakov*

*B.P. Konstantinov Petersburg Nuclear Physics Institute*

INTEGRAL PROMPT NEUTRON SPECTRA FOR THERMAL-NEUTRON INDUCED FISSION OF U-235. Fission neutron energy spectra were measured for $^{235}$U and $^{252}$Cf. Measurements were made simultaneously at 11 angles between the flight paths of the outgoing neutrons and the outgoing light fragments. The flight paths of the light fragments were determined using multi-wire proportional counters. Neutron energy was determined by the time-of-flight method. Neutrons and γ-quantum events were separated using discrimination by impulse shape. The data were analysed to obtain the ratio of the integral spectra for the $^{235}$U(*n,f*) and $^{252}$Cf(*s.f*) reactions. The integral fission neutron spectrum for $^{235}$U(*n,f*) was determined from this ratio by assuming a fission neutron spectrum for $^{252}$Cf(*s.f*) of standard shape.

## Introduction

Measurements made by us previously of the angular and energy distributions of prompt neutrons from fission of $^{235}$U(*n,f*) by neutrons at an energy of 0.0363 eV showed that the yield of neutrons emitted before and at the moment of scission of the fissioning atom and, possibly, at the initial stage of fragment acceleration, can make up no more than 5% of the total number of neutrons per fission [1]. In addition, the angular dependence of the yield and average energy of prompt fission neutrons depends weakly on the shape of the integral fission neutron spectrum for $^{235}$U(*n,f*). The greatest uncertainty in the dependencies obtained (approx. 3–5%) — that due to uncertainty in the shape of the integral spectrum — is observed at angles in the vicinity of 90% [2]. Given a precision better than 2% for the experimental data, it appears reasonable to measure the shape of the integral prompt fission neutron spectra for $^{235}$U(*n,f*) in order to exclude this uncertainty when analysing the distributions obtained.

The current internationally accepted standard for such measurements is the integral prompt neutron spectrum for the spontaneous fission reaction $^{252}$Cf(*s.f*) [3]. Despite this, there is a clear shortage of experimental data on the angular and energy distributions of fission neutrons for $^{252}$Cf(*s.f*) containing numerical data. There are only two collections of such data in the literature [4, 5]. For this reason, the angular and energy distributions of the prompt fission neutrons for $^{235}$U(*n,f*) were measured in relation to the spontaneous fission reaction $^{252}$Cf(*s.f*) under identical experimental conditions using an experimental set-up employed previously for such measurements [1]. This made it possible to obtain not only the integral neutron spectrum for $^{235}$U(*n,f*) but also angular and energy distributions for $^{252}$Cf(*s.f*) that are required in order to verify and advance current understanding of the mechanism by which prompt fission neutrons are emitted.

* Translated from Voprosy Atomnoj Nauki i Tekniki Ser. Yadernye Konstanty, No. 1-2, pp. 37-54, 2011-2012.

**Measurement method**

The experiment was carried out using radial neutron channel No. 7 at the VVR-M reactor (B.P. Konstantinov Petersburg Nuclear Physics Institute, Gatchina) equipped with a low-background reflecting neutron guide 3 m in length. The neutron flux density (average energy 0.0363 eV) at the exit slit of the neutron guide, which measured 3×40 mm, was approximately $2 \cdot 10^7$ $cm^{-2} \cdot c^{-1}$. During measurements of the fission neutron spectra for $^{235}U(n,f)$ ('beam on' mode), the neutron beam travelled along an evacuated tube, passed through a 100 μ-thick aluminium window in the reaction chamber and struck the target, which was positioned in the centre of the chamber, at a small angle. In the set-up for spontaneous fission ('beam off' mode), a $^{252}Cf$ target was positioned in the centre of the chamber in place of the $^{235}U$ target. The chamber, which had a diameter of 350 mm, was made from duraluminium and had walls 2 mm thick. During measurements the chamber was filled with isobutane to a pressure of 4 mm Hg.

In the experiment described here, the $^{235}U$ target, a spot 15 mm in diameter and 280 μg/$cm^2$ thick, was applied to a self-supporting substrate of $Al_2O_3$ 70 μg/$cm^2$ thick.

A layer of $^{252}Cf$ with an activity of $3 \cdot 10^4$ fissions per second and a diameter of 10 mm was fabricated using the method of self-sputtering in a vacuum onto a stainless steel substrate 0.18 mm thick.

The prompt fission neutron spectra were measured simultaneously for 11 angles between the neutron's flight path and the direction of the light fragment: 0°, 18°, 36°, 54°, 72°, 90°, 108°, 126°, 144°, 162° and 180°. Adjusting for the actual geometry and angular resolution of the experimental set-up, these angles measured 8.8°; 19.8°; 36.9°; 54.5°; 72.2°; 90°, 107.8°; 125.5°; 143.1°; 160.2° and 171.2°, respectively. The measurements were performed using an experimental set-up [1] designed as shown in Figure 1. The energy of the fission neutrons and the velocity of the fission fragments were determined by time of flight.

The start signal used was the fission fragment pulse generated by a multi-wire proportional counter (MWPC) 3.5 mm thick located 3.5 mm away from the fissioning target (at the near surface of the detector), parallel to the target plane. It sensitive surface area measured 20×92 mm. The start MWPC with ring (target holder) was mounted on a special frame installed in the centre of the reaction chamber so that all the hardware was outside the path of the neutron beam. Detection efficiency for fission fragments entering the sensitive volume of the start MWPC is entirely a function of the start counter's 'incoming' transparency; in this case it was 97%. The start counter's overall transparency was on average approx. 82%.

Fission neutrons passed through a 0.1 mm-thick aluminium window in the side of the chamber and were detected by means of two neutron detectors (Ø50×*h*50 mm and Ø60×*h*40 mm stilbene crystals with Hamamatsu-R6091 photomultiplier). The neutron detectors were positioned at 90° to one another at a distance from the target fissioning material of $d_1$ = 49.2 ±0.3 cm and $d_2$ = 47.2 ±0.3 cm, respectively. The solid angles subtended by the neutron detectors as seen from the source measured 0.008 ±0.001 and 0.013 ±0.001 steradians, respectively. The neutron detectors were placed in cylindrical shielding consisting of 30 mm of lead and 40 mm of polyethylene. The neutron detection threshold was 150–200 keV. To separate neutron and γ-quantum events, two forms of discrimination were used (by pulse shape and by time of flight).

To determine the direction of the fission fragments, stop MWPCs were used that had a thickness of 3 mm, a working surface area of 72×38 mm and a permeability of 97.5%. There were sixteen MWPCs in the reaction chamber, which was filled with isobutane (approx. 4 mm Hg), arranged in two arcs (of

8 counters each) in pairs located radially opposite each other at a distance of 140 mm from the fissioning target. The working voltage of all the MWPCs was 400–500 V. The neutron beam producing the fission passed along the chamber's axis perpendicular to the plane in which were positioned all the detectors for detecting fragments (the stop MWPCs) and fission neutrons (the two stilbene crystals with photomultiplier).

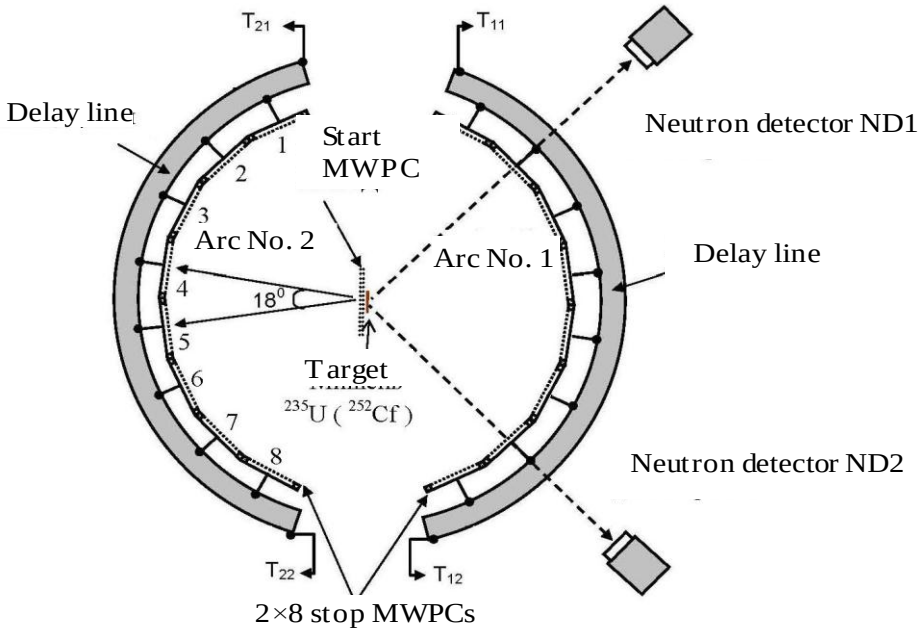


Fig. 1. General view of the experimental set-up.
The neutron beam producing the fission is perpendicular to the plane of the figure.

**Measurement procedure**

The measurements were performed in two-week cycles. During each cycle, measurements were made alternately of the angular and energy distributions of the prompt fission neutrons for $^{235}$U(*n,f*) and $^{252}$Cf(*s.f*). The $^{252}$Cf(*s.f*) target was positioned in the reaction chamber in the same place as the $^{235}$U(*n,f*) target. Four cycles of measurements were completed.

A schematic diagram of the experiment is shown in Fig. 2. Data collection and control was performed using a PC (running Linux) with a data acquisition system using the CAMAC standard. The signals from the start and stop MWPCs for fission fragments, along with those from the anodes of the photomultipliers of the two neutron detectors, after pre-amplification and shaping (TFA), were sent to discriminators (CFD) and then to time-to-digital converters (TDC). To separate neutron and γ-quantum events, the signals from the neutron detectors were also sent to independent inputs on a charge-to-digital converter (CDC), where for each pulse from a neutron detector in a window of 300 ns the complete (PH) and partial (PS) integral were measured. The window for the partial integral opened with a delay of approx. 30 ns with respect to the window in which the complete integral was measured. Strictly speaking, the precision of the CFD timing depends on the amplitude of the signal being applied to its input. For this reason, the complete integrals of the pulses from the

start MWPC (PF 1) and the stop MWPCs on arc No. 1 (PF 2) and on arc No. 2 (PF 3) were also measured using a CDC.

During the measurements, all fission events accompanied by a pulse from the start MWPC were recorded. Whenever the signals from at least one of the neutron or fragment detectors coincided with the signal from the start MWPC within the 300 ns-window, the data was read from the TDCs (channel time width 0.05 ns) and CDC and put in the PC's working memory. Events involving fission without detection of neutrons or γ-quanta were read into the PC's working memory with a counting coefficient of 1:50. When the reading of the data was completed a control signal was generated (output register in Fig. 2) that was used to zero all the modules.

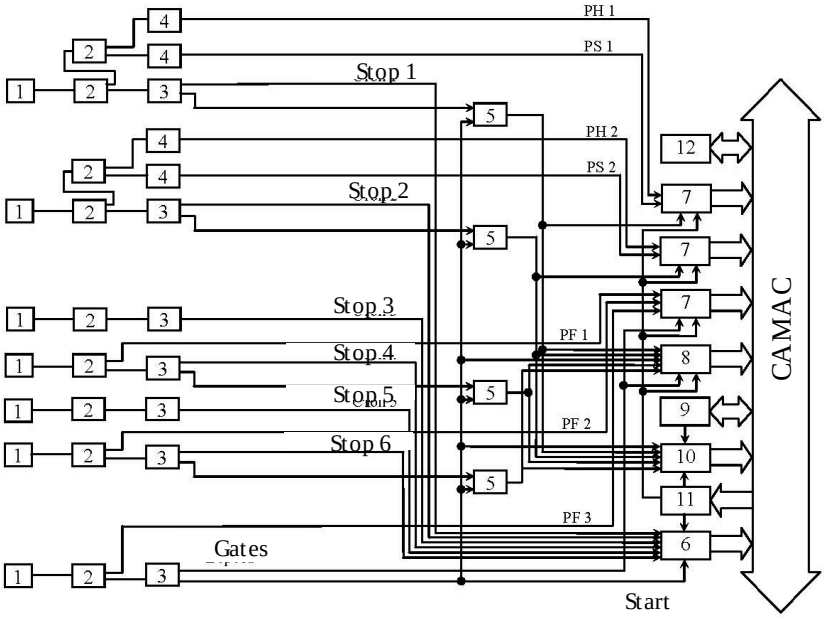


Fig. 2. Schematic diagram of the experiment:
1 — pre-amplifier (PA); 2 — fast amplifier-shaper (TFA); 3 — tracking-threshold discriminator (CFD); 4 — delay line; 5 — coincidences circuit; 6 — single-stop time coder (TDC); 7 — charge-to-digital converter (CDC); 8 — coincidences register; 9 — clock; 10 — monitoring counter; 11 — output register (); 12 — personal computer

For monitoring in real time, every ten seconds the data read from the monitoring counters were displayed on the monitor screen. The monitoring counters received the counts from the start counter (total number of fissions), the number of output signals (number of events processed during acquisition, which for a dead time of zero should coincide with the total number of fissions), the number of triggerings on each arc of MWPCs, and the number of coincidences with events detected by the neutron detectors. To enable off-line processing, the data from these monitoring counters were also written to the PC's hard disk. The stability of the equipment's operation was monitored more closely by periodically observing the count parameters and the position and half-width of the peaks corresponding to the light and heavy fragment groups in the fission fragment time-of-flight spectra and those corresponding to the fission γ-quanta in the neutron time-of-flight spectra. Additional monitoring of the stability of the discrimination thresholds in the neutron and fragment channels was achieved by using the corresponding amplitude distributions.

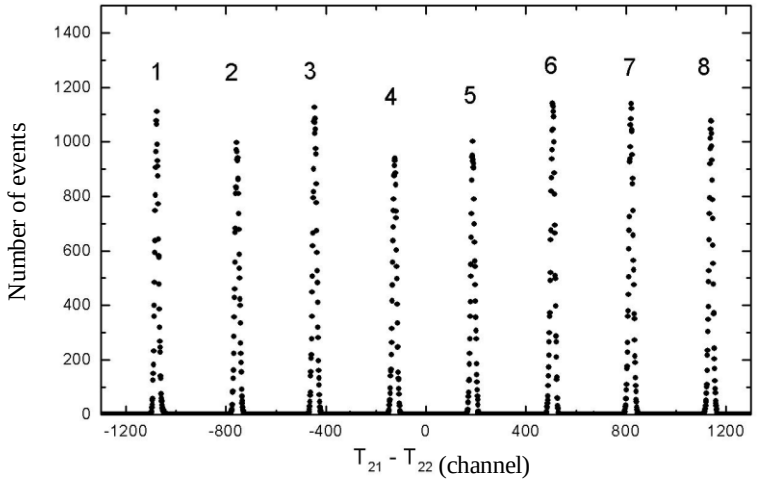


Fig. 3. Number of $^{252}$Cf(*s.f*) fission events detected as a function of the difference in the time of arrival at the two ends of the delay line of the pulse from the stop MWPCs (the numbering of the peaks from 1 to 8 corresponds to the stop MWPCs shown in Fig. 1)

The information on a detected event included: the event code (fission event or monitoring count); the amplitudes of the signals from the start detector and stop detectors for fragments (PF1, PF2 and PF3); the complete and partial integrals from the two neutron detectors (PH1 and PS1; PH2 and PS2); the time of flight of the fragments from the two ends of the delay line for arc No. 1 ($T_{11}$, $T_{12}$) and arc No. 2 ($T_{21}$, $T_{22}$); the time of flight of the neutron for the two neutron detectors ($T_1$ and $T_2$) and the event attribute, which contained information on the type of event detected (fragment, fragment-neutron, fragment-fragment, fragment-fragment-neutron, neutron).

In this experiment the position in space of the neutron detectors was fixed. The relative exit angles of the neutrons are given by the position of the fragment stop detector that detected the fission event being analysed. The position of that detector is determined from the difference in the arrival times of the pulse from the fragment detector at the two ends of the delay line connected to the output of each of the 8 MWPCs on arc No. 2 only (Fig. 3). Since the target for $^{252}$Cf(*s.f*) was applied to a substrate that is opaque to fission fragments, the fission events analysed were those detected by the stop MWPCs positioned on arc No. 2.

**Processing of the experimental data**

The experimental set-up as built ensured identical conditions (magnitude and make-up of the background, neutron detector efficiency and neutron rescattering by the parts of the set-up) for measuring the neutron spectra at different angles to the directions of the fragments.

The data from each cycle of measurements were processed independently for the two neutron detectors. The procedure for the preliminary processing of the measured time-of-flight spectra for the 11 chosen angles relative to the direction of the light fragment, θ, consisted in applying a series of corrections to the source data. The procedure for applying the corrections has been described in some detail in our earlier publication [1]. Analysis of the data obtained in [1] showed [2] that additional corrections need to be applied to the measured distributions of the prompt fission neutrons, and the procedure for applying the corrections must be changed. The main stages in the processing of the experimental data are described below. Special attention was given

to the corrections for which the procedure of application was changed; these concern effects related to the finite angular and energy resolution of the experimental set-up and to the fact that the quantities being observed in the experiment have a discrete rather than a continuous distribution.

Correction for timing errors in measuring time-of-flight spectra. This correction was applied to eliminate a dependency between the signal amplitude and the position of the corresponding time mark in the start and stop channels detecting fission fragments and in the neutron channels. In addition, the difference in the flight times of the heavy and light fragments from the target to the start detector was taken into account. Applying in turn the corrections listed above to the time-of-flight spectra for neutrons and for γ-quanta reduced the full width at half maximum of the peak for 'fragment-γ-quantum' coincidences from approx. 2.5 ns to 1–1.2 ns.

Correction for neutron detector background. In order to reliably separate neutron and γ-quantum events, pulse shape discrimination was used; this made it possible to suppress the γ-background by a factor of about 200. Next, the neutron time-of-flight spectra obtained were corrected by subtracting the background component due to random coincidences between a fragment and a neutron belonging to different fission events [6]. To determine the background of neutrons scattered by structural materials located outside the solid angle of detection, a series of measurements was performed with a shadow cone. The shadow cone was made of steel and was 10 cm long. After accounting for the scattered neutron background, a correction had to be applied for the time-independent background of random coincidences and for the background due to incomplete separation of neutron and γ-quantum events (for neutron energies below 0.5 MeV) and to neutrons scattered within the solid angle of detection. The proportion of the latter increases as neutron energy decreases. For this reason, the residual background component was arrived at by linear interpolation from the average values for the left edge (number of events before the peak of fragment-γ-quantum coincidences) and for the right edge (number of events in channels exceeding the discrimination threshold in the neutron channels) of the time-of-flight spectra.

The contribution of the background after discrimination of events by pulse shape, averaged over all angles, did not exceed 8% of the number of neutron events remaining after all background components were subtracted. For example, the proportion of such events in the time-of-flight spectra for the prompt fission neutrons detected at 8.9° and 90° to the axis of fission was less than 1% and approx. 7%, respectively.

Correction for fragment detector efficiency. To reduce the fission neutron spectra to the same solid angle for fragment detection, the number of fission fragments detected by each of the 8 stop MWPCs on arc No. 2, $N_f(\theta)$, was measured. The differences in the solid angles of detection did not exceed ±4% (Fig. 3). Looking at the spectra of the specific losses of fragments (PF 1 and PF 3) in the gas-filled cathode-to-anode gap in the MWPCs (Fig. 4), one can see that significantly different values were obtained for the complete integral of the pulse from the MWPCs for fission fragments and α-particles. Thus, fission fragment events can be separated out by introducing a detection threshold without any loss of efficiency in fission fragment detection.

Correction for the contribution of an additional fragment due to incomplete fission of light and heavy groups of fragments. In this paper, for the separation of the light and heavy fragment time-of-flight spectra were used that were obtained by sorting the events detected by the MWPCs on arc No. 2 and those in which there was fission without detection of neutrons. The boundary separating the light and heavy fragment groups was defined as the local minimum on the corresponding time-of-flight spectrum (Fig. 5). With this approach to separation, some of the heavy fragments are interpreted as light fragments and vice versa. We note that the time-of-flight spectra

obtained can be described fairly precisely as the sum of two Gaussian distributions corresponding to the light and heavy fragment groups. Thus, the proportion of events being misinterpreted can be found by taking the portion of the corresponding Gaussian distribution below (for light fragments) or above (for heavy fragments) the line of separation. Determined in this way, the proportion of heavy fragments in the light group was 1–2% and 6–9% for $^{235}$U(*n,f*) and $^{252}$Cf(*s.f*), respectively.

It is worth noting that the application of this correction slightly alters the ratio of the neutrons emitted by the light and the heavy fragments without changing the integral prompt fission neutron spectrum.

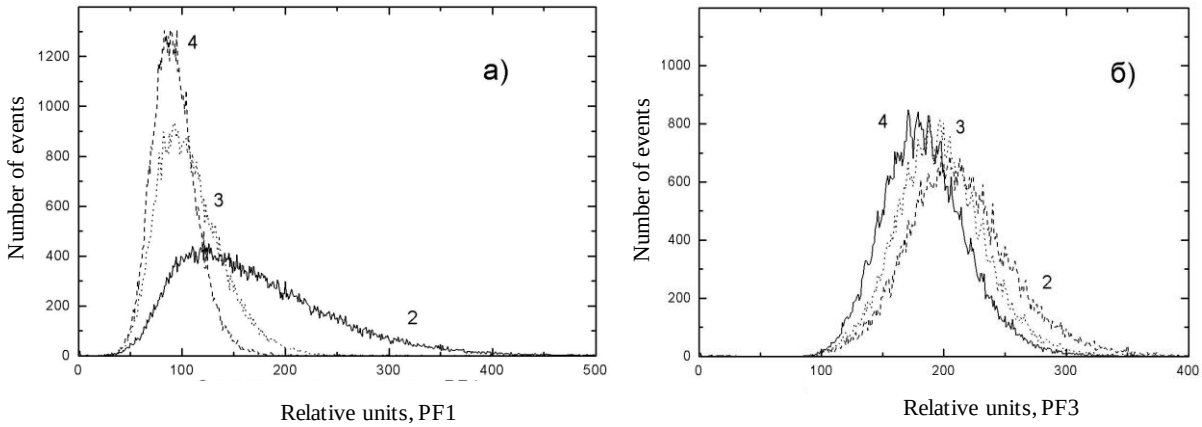


Fig. 4. Spectra of specific losses of fission fragments for $^{235}$U($n_{th}$, *f*) in the gas-filled cathode-to-anode gap in the start MWPC (*PF* 1) (a) and the stop MWPCs (*PF* 3) (b) for events detected by stop MWPCs 2, 3 and 4 on arc No. 2 (Fig. 1).

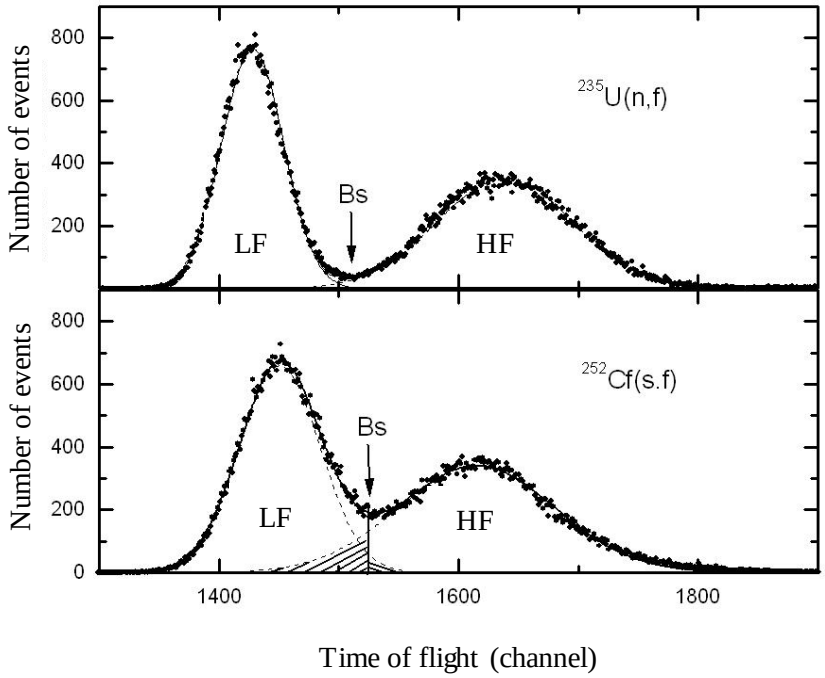


Fig. 5. Fission fragment time-of-flight spectra for $^{235}$U($n_{th}$, *f*) and $^{252}$Cf(*s.f*): Bs — boundary separating the light and heavy fragment groups.

Correction for the angular and energy distribution of fission neutrons for $^{235}$U(*n,f*) and $^{252}$Cf(*s.f*). In order to increase the statistical precision of the data obtained, and bearing in mind that the channel width of the time coder was 0.05 ns as against a total time resolution in the neutron channel of approx. 1 ns, all neutron time-of-flight spectra $n(t, \theta)$ were obtained from instrumental spectra corrected for the effects described above by summing across 20 channels. The number of neutrons with energy $E_n$ per fission that were detected in a single energy interval at angle θ to the direction of the light fragment in the laboratory system per unit of solid angle, $n(E_n, \theta)$, was obtained from the measured time-of-flight spectra $n(t, \theta)$ corrected for the effects described above by means of expressions (1) and (2):

$$n(E_n, \theta = n(e_n, \theta) \cdot \left[1 - 2 \cdot \frac{e_n}{m_n c^2}\right]^{3/2}, \quad n(e_n, \theta) = n(t, \theta) \cdot \frac{t}{e_n \cdot \Omega \cdot N_f(\theta)} \tag{1}$$

where $e_n$ is the energy of the neutron in non-relativistic approximation, in MeV; $D$ is the flight distance, in m; $t$ is the time is takes the neutron to cover distance $D$, in ns; Ω is the solid angle subtended by the detector as seen from the fissioning target, in steradians; $m_n c^2$ is the rest energy of the neutron, 939.565 MeV; and $E_n$ is the energy of the neutron in relativistic approximation, in MeV, determined using the formula:

$$E_n = m_n c^2 \cdot \left[(1 - 2 \cdot \frac{e_n}{m_n c^2})^{-1/2} - 1\right], \quad e_n = \left(\frac{72.288 \cdot D}{t}\right)^2. \tag{2}$$

Correction for the angular and energy resolution of the experimental set-up. The resolution of the set-up used in this work was limited with respect to both the angle and the energy of the neutrons detected. For this reason, the following corrections had to be applied to the measured distributions $n(E_n, \theta)$. In the general case, to determine the desired differential neutron spectrum $N(E_n, \theta)$ requires solving an integral equation of the following form:

$$n(E_n, \theta) = \iint F_\theta(\theta, \theta' : E_n)\, F_E(E_n, E' : \theta)\, N(E', \theta')\, dE' d\theta', \tag{3}$$

where $F_\theta(\theta, \theta')$ and $F_E(E_n, E')$ are functions for the experimental set-up's angular resolution and the energy resolution of the neutron detector, respectively.

The function for angular resolution, $F_\theta(\theta, \theta')$, was calculated from the actual geometry of the experiment, as shown in Fig. 6. It was assumed that the function for the energy resolution at a constant detected neutron energy, $F_E(E_n, E')$, can be represented as a Gaussian distribution having a variance $\sigma_E^2$ given by the expression:

$$\Delta E_n = 2.35 \cdot \sigma_{E'}(E_n), \quad \frac{\Delta E_n}{E_n} = 2 \cdot \sqrt{(\frac{\Delta t}{t})^2 + (\frac{\Delta D}{D})^2}, \quad D = d + \frac{h}{2}, \tag{4}$$

$$\Delta D = 2.35 \cdot \delta D' \text{ and } (\delta D')^2 = \frac{h^2}{12} + \frac{(\delta d)^2}{3} \tag{5}$$

where $\Delta E_n$ is the full width at half maximum; $d$ and $\delta d$ are the flight path and its geometric uncertainty; $h$ is the height of the stilbene crystal; $\Delta D$ is the total uncertainty of the flight path; $\Delta t$ is the total measurement uncertainty for the neutron's time of flight over a fixed flight path $D$. The total uncertainty $\Delta t$ is the sum of the uncertainty in the neutron and fragment time-of-flight measurements, the uncertainty in the fragment's time of flight to the start detector and the uncertainty in the width of the timing channel. In using expression (4) it was assumed that $\Delta t$ was constant over the entire range of measured flight times, that it was independent of the energy of the detected neutron and γ-quantum and that it was equal to the full width at half-maximum of the

peak for ‘fragment-γ-quantum’ coincidences. Fig. 7 shows the calculated relative error for the two neutron detectors used, as a function of the energy of the neutron detected.

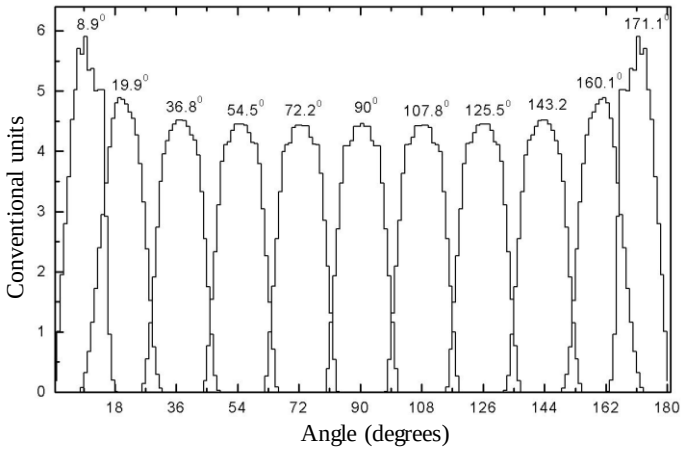


Fig. 6. Angular resolution function calculated from the actual geometry of the experiment.

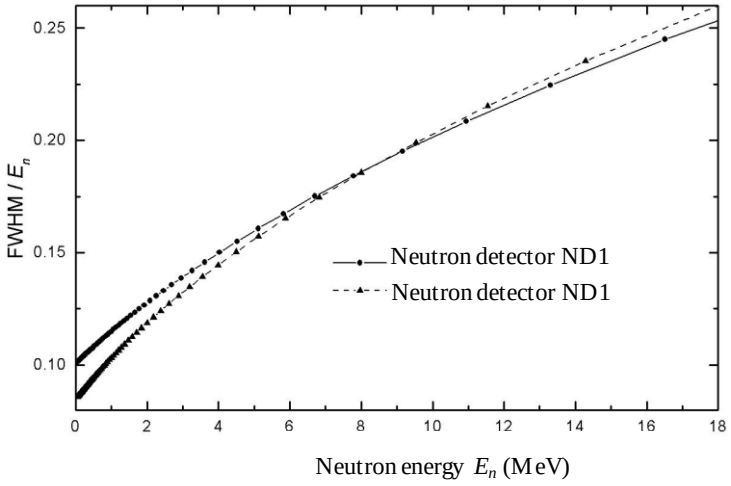


Fig. 7. Function for the energy resolution of the neutron detectors.

Solving equation (3) presents certain difficulties, since it belongs to the class of ‘ill-conditioned’ problems. Such problems have the property that arbitrarily small changes to the initial data can result in arbitrarily large changes in the solution. Therefore, to take into account the effects described above an indirect method was used and the data were processed in the manner described below.

It will be recalled that the experimentally observed angular and energy distributions of fission neutrons can be described with a precision approaching 10% by a model in which the neutrons are emitted by fully accelerated fragments (see for example [2, 5 and 7]). Given this, an initial approximation for the desired differential spectrum $N_0(E', \theta')$ for each fixed angle θ was obtained by using distributions calculated from the measured distributions $n(E_n, \theta)$ assuming neutron emission from fully accelerated fragments [1, 2]. For this purpose, the calculations were performed on a uniform grid with a spacing of 0.01 MeV for energy and 1° for the angle of the neutron detected. Next, by substituting $N_0(E', \theta')$ in expression (3), fission neutron spectra were obtained which were distorted owing to the angular resolution of the experimental set-up and the energy resolution of the neutron detector $n_0^V(E', \theta')$. The next approximation of the desired

distribution $N_1(E', \theta')$ was also calculated assuming emission of fission neutrons by fully accelerated fragments. The initial distributions used for the calculation were the measured distributions corrected for angular and energy resolution, $n'(E_n, \theta)$, using the expression:

$$n'(E_n, \theta) = n(E_n, \theta) \cdot \frac{N_0(E_n,\theta)}{n_0^V \cdot (E_n,\theta)}, \quad (6)$$

As a result, final corrections for resolution were obtained in the form of factors to be applied to the measured distributions $n(E_n, \theta)$ and were defined as the ratio of $N_1(E', \theta')$ to the result obtained by substituting $N_1(E', \theta')$ in expression (3) $n_1^V(E', \theta')$. Then

$$N_x(E_n, \theta) = \left[\frac{N_1(E_n,\theta)}{n_1^V(E_n,\theta)}\right]_x \cdot I_x(E_n) \cdot B_x(E_n) \cdot n_x(E_n, \theta) = F_x(E_n) \cdot n_x(E_n, \theta), \quad (7)$$

$$F_x(E_n) = f_x^E(E_n, \theta) \cdot f_x^\theta(E_n, \theta) \cdot I_x(E_n) \cdot B_x(E_n), \quad (8)$$

where $x$ is the target index ($x$ = U or Cf); $f_x^E(E_n{:}\,\theta)$ and $f_x^\theta(E_n{:}\,\theta)$ are the corrections for angular and energy resolution, respectively; $I_x(E_n)$ is the correction for the summing effect due to the fact that the experimentally observed quantities have discrete distributions; $B_x(E_n)$ is a correction having to do with the finite width of the energy intervals of the grid on which the neutron spectra were determined. The values of the corrections obtained for $^{235}$U($n,f$) and $^{252}$Cf($s.f$) are shown in Figs 8–10. After applying the corrections described above for each neutron detector differential fission neutron spectra were obtained for $^{235}$U($n,f$), $N_U(E_n,\theta)$, and for $^{252}$Cf($s.f$), $N_{Cf}(E_n,\theta)$, which require correction for neutron detector efficiency.

a)

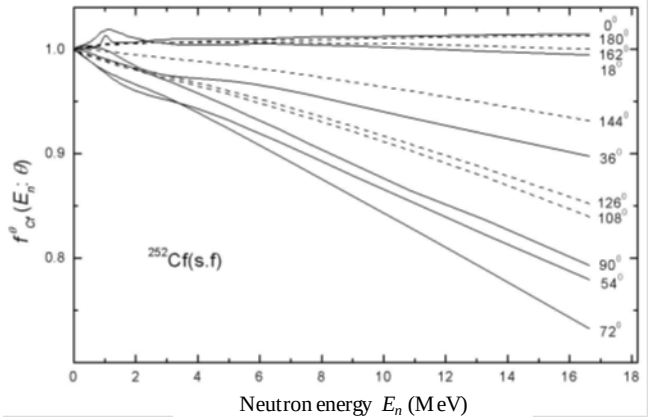


b)

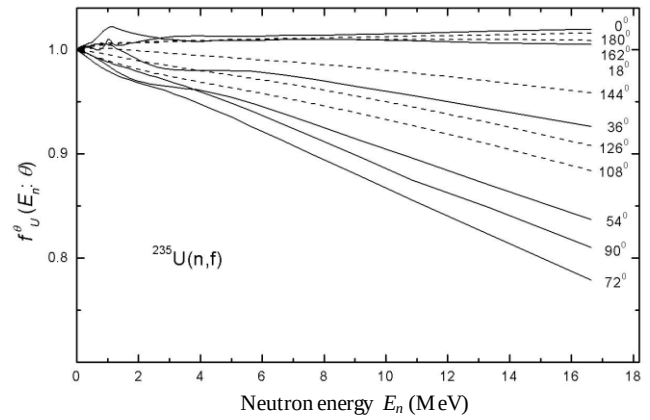


Fig. 8. Calculated value of the correction for angular resolution to the measured fission neutron spectra for $^{252}$Cf($s.f$) (a) and $^{235}$U($n_{th}$, $f$) (b) for fixed angles θ relative to the direction of the light fragment. Solid line — light fragment; dotted line— heavy fragment.

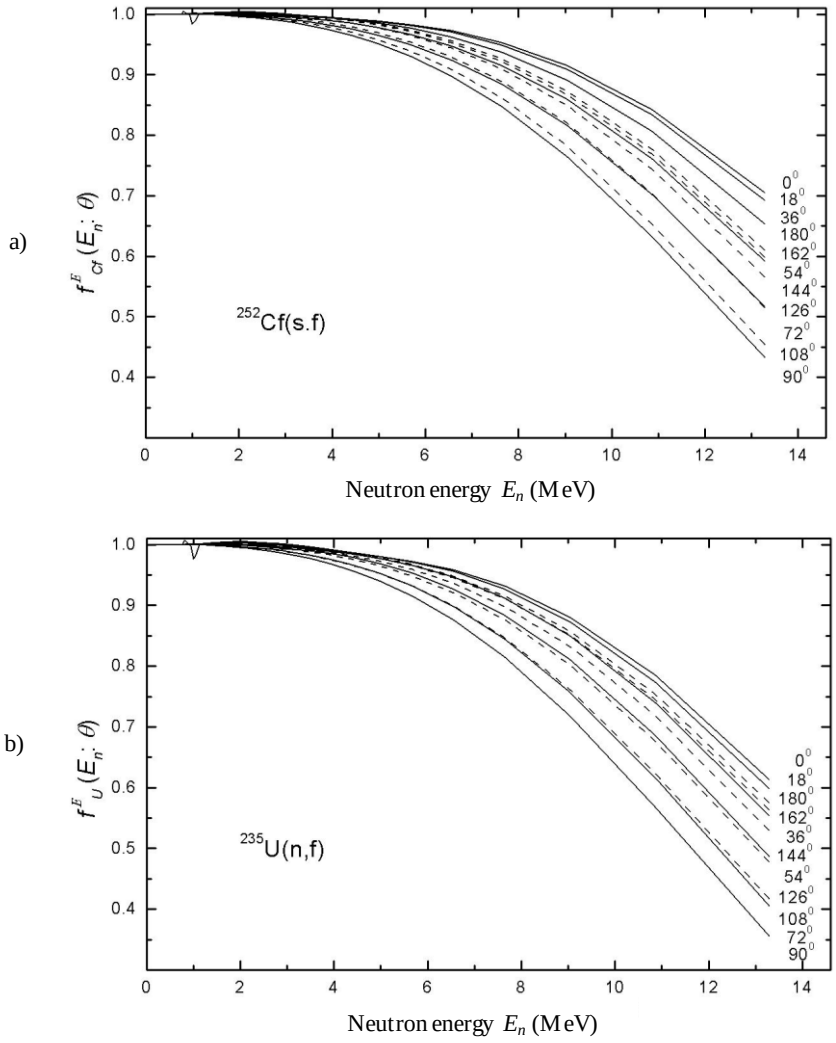


Fig. 9. Calculated value of the correction for energy resolution to the measured fission neutron spectra for $^{252}$Cf(*s.f*) (a) and $^{235}$U($n_{th}$, *f*) (b) for fixed angles θ relative to the direction of the light fragment. Solid line — light fragment; dotted line— heavy fragment.

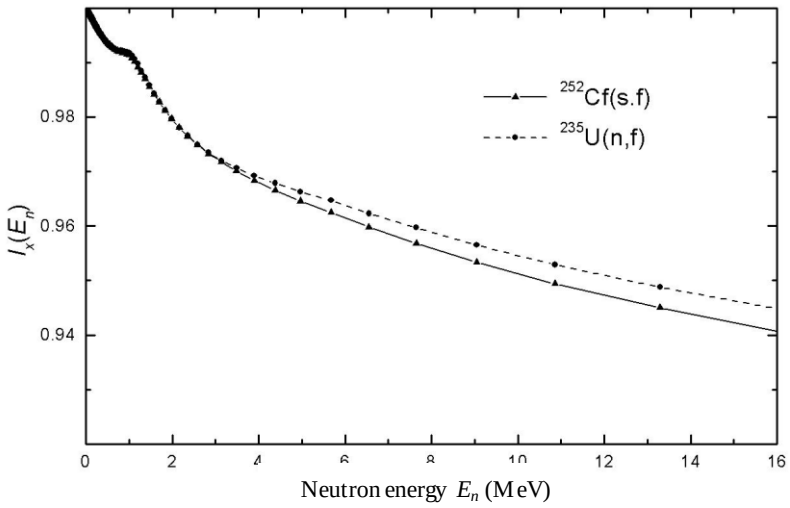


Fig. 10. Calculated value of the summing effect correction to the integral fission neutron spectra for $^{235}$U($n_{th}$, *f*) and $^{252}$Cf(*s.f*).

Correction for neutron detector efficiency. Integral fission neutron spectrum for $^{235}$U(*n,f*).
The current internationally accepted standard for the measurement of fission neutron spectra is the integral prompt neutron spectrum for the spontaneous fission reaction $^{252}$Cf(*s.f*), $N_{Std}(E_n)$ [3]. For this reason, the angular and energy distributions of prompt fission neutrons for $^{235}$U(*n,f*) were measured in relation to the spontaneous fission reaction $^{252}$Cf(*s.f*) under identical experimental conditions.

Thus, the number of neutrons having energy $E_n$ per fission that are emitted in a single energy range at angle θ to the direction of the light fragment in the laboratory system per unit solid angle, corrected for neutron detector efficiency, $\Phi_x(E_n, \theta)$, is equal to:

$$\Phi_x(E_n,\theta) = \frac{N_{Std}(E_n)}{N_{Cf}(E_n)} \cdot N_x(E_n,\theta) = \varepsilon(E_n)^{-1} \cdot N_x(E_n,\theta), \quad (9)$$

$$N_x(E_n) = 2\pi \cdot \int_0^{\pi} N_x(E_n,\theta)\sin(\theta)d\theta, \quad (10)$$

where $\varepsilon(E_n)$ is the neutron detector efficiency and $N_{Cf}(E_n)$ is the integral prompt fission neutron spectrum for $^{252}$Cf(*s.f*) obtained by means of expression (10). Consequently, assuming that the density distribution of the prompt fission neutrons relative to the axis of fission in the laboratory system is symmetric, the desired integral prompt fission neutron spectrum (*x* = U or Cf) can be determined by means of expression (11):

$$\Phi_x(E_n) = 2\pi \cdot \int_0^{\pi} \Phi_x(E_n,\theta)\sin(\theta)d\theta. \quad (11)$$

It is also possible to obtain the ratio $R(E_n)$ of the integral spectra for $^{235}$U(*n,f*) and $^{252}$Cf(*s.f*), which is not affected by uncertainty due to imprecision in determining the length of the flight path and in determining the channel width of the time coder (TDC). Since in the present work the integral spectra were measured under identical conditions using the same measuring equipment and the data were then processed in the same way for both nuclei being studied, the effects due to neutron scattering by the structural material of the set-up should be suppressed to a significant degree in the ratio $R(E_n)$ to be obtained.

The ratio $R(E_n)$ to be obtained is also unaffected by systematic errors in determining neutron detector efficiency, meaning it is not sensitive to assumptions concerning the nature of the spectrum for $^{252}$Cf(*s.f*), $N_{Std}(E_n)$.

Hence in what follows, the result of measurements of the spectrum for $^{235}$U(*n,f*) is expressed in terms of the ratio $R(E_n)$, as this makes it possible not only to minimize the uncertainty in the data obtained but also to determine the integral spectrum for $^{235}$U(*n,f*) from the current standard, $N_{Std}(E_n)$, by means of expression (12):

$$R(E_n) = \frac{\Phi_{\mathrm{U}}(E_n)}{\Phi_{\mathrm{Cf}}(E_n)} = \frac{\Phi_{\mathrm{U}}(E_n)}{N_{Std}(E_n)\cdot \nu_{\mathrm{Cf}}} = \frac{N_{\mathrm{U}}(E_n)}{N_{\mathrm{Cf}}(E_n)} = F(E_n) \cdot \frac{n_{\mathrm{U}}(E_n)}{n_{\mathrm{Cf}}(E_n)}, \quad (12)$$

$$n_x(E_n) = 2\pi \cdot \int_0^{\pi} n_x(E_n,\theta)\sin(\theta)d\theta, \quad (13)$$

where $\Phi_{\mathrm{U}}(E_n)$ and $\Phi_{\mathrm{Cf}}(E_n)$ are the desired integral fission neutron spectra; $\nu_{\mathrm{Cf}}$ is the recommended average whole number of prompt neutrons per fission for $^{252}$Cf(*s.f*) ($\nu_{\mathrm{Cf}}$ = 3.759; ENDF/B-VII); $N_{\mathrm{U}}(E_n)$ and $N_{\mathrm{Cf}}(E_n)$ are the integral fission neutron spectra obtained by applying all the corrections described above except the correction for neutron detector efficiency; $n_{\mathrm{U}}(E_n)$ and $n_{\mathrm{Cf}}(En)$ are the integral fission neutron spectra obtained from the measured differential spectra $n(E_n, \theta)$ for $^{235}$U(*n,f*) and $^{252}$Cf(*s.f*), respectively; $F(E_n)$ is the total correction to the experimentally measured ratio of the integral spectra. The total correction $F(E_n)$ can be represented as the product in (14):

$$F(E_n) = f_{res}^{E}(E_n) \cdot f_{res}^{\theta}(E_n) \cdot I(E_n) \cdot B(E_n), \tag{14}$$

$$I(E_n) = \frac{I_U(E_n)}{I_{Cf}(E_n)}, \quad B(E_n) = \frac{B_U(E_n)}{B_{Cf}(E_n)}, \tag{15}$$

where $f_{res}^{\theta}(E_n)$ and $f_{res}^{E}(E_n)$ are a coefficient defined as the ratio of the integral spectra under study obtained before the application of corrections, to this ratio after correction for angular and energy resolution, for $^{235}$U(*n,f*) and $^{252}$Cf(*s.f*) respectively.

The corrections $I_x(E_n)$ were defined as the ratio of the integral spectra for the substance *x* under study that were obtained by integrating over angle, using Simpson's method, an expression analogous to expression (9) with intervals of 1 and 18 degrees, respectively. For this the neutron angle and energy distributions used under the integral in expression (9) were calculated assuming that all fission neutrons are emitted by fully accelerated fragments. Since this describes the experimental data with a precision of 10% or better, a correction for the difference between the true and the calculated distributions would be a second-order infinitesimal.

The integral fission neutron spectra $n_x(E_n)$ (*x* = U or Cf) were determined independently for each of the two neutron detectors as a weighted average of the four independent measurement cycles:

$$n_{xk}(E_n) = \frac{\sum_{i=1}^{m} n_{xki}(E_n) \cdot \left(\frac{1}{\Delta n_{xki}(E_n)}\right)^2}{\sum_{i=1}^{m} \left(\frac{1}{\Delta n_{xki}(E_n)}\right)^2}, \quad \Delta n_{xki}(E_n) = \sqrt{\frac{\sum_{l=1}^{20} \left(n_{xki}^{*}(l,E_n) - n_{xki}(E_n)\right)^2}{20}}, \tag{16}$$

where *i* is a particular measurement cycle (the number of measurement cycles *m* = 4); k is the number of the neutron detector; $\Delta n_{xki}(E_n)$ is the error for the integral spectrum $n_{xki}(E_n)$ obtained in the i-th measurement cycle for the k-th neutron detector; $n_{xki}^{*}(l, E_n)$ is the *l*-th excited integral spectrum of the corresponding $n_{xki}(E_n)$ integral spectrum. Each *l*-th excited integral spectrum $n_{xki}^{*}(l, E_n)$ was obtained from measured time-of-flight spectra $n_{xki}(t, \theta)$, in which the number of counts in each channel varied within the limits of the statistical precision achieved $n_{xki}(t, \theta) \pm (n_{xki}(l, t, \theta))^{1/2}$.

It was assumed that the errors in the various channels for each measured spectrum are uncorrelated and dispersion was random. The errors so defined include, in addition to statistical imprecision, uncertainties related to imprecision in the determination of time zero and instability in the operation of the electronic equipment. The uncertainty in the corrections for the summing effect and for angular and energy resolution are also part of the error obtained in this way, since these corrections were determined independently for each cycle of measurements. Preliminary analysis revealed that there was a minor systematic difference of approx. 1.4% between the ratios $R(E_n)$ obtained for the two neutron detectors. After incorporating the measurements with the shadow cone, this uncertainty disappeared. The final integral spectra $n_U(E_n)$ and $n_{Cf}(E_n)$, averaged over the two neutron detectors, were obtained by means of the expressions:

$$n_x(E_n) = \frac{n_{x1}(E_n) \cdot \left(\frac{1}{\Delta n_{x1}(E_n)}\right)^2 + n_{x2}(E_n) \cdot \left(\frac{1}{\Delta n_{x2}(E_n)}\right)^2}{\left(\frac{1}{\Delta n_{x1}(E_n)}\right)^2 + \left(\frac{1}{\Delta n_{x2}(E_n)}\right)^2}, \tag{17}$$

$$\Delta n_x(E_n) = \sqrt{\frac{1}{\left(\frac{1}{\Delta n_{x1}(E_n)}\right)^2 + \left(\frac{1}{\Delta n_{x2}(E_n)}\right)^2}}, \quad D_x = \frac{\Delta n_x(E_n)}{n_x(E_n)}, \tag{18}$$

where $D_x$ is the relative measurement error for the integral prompt fission neutron spectrum for $^{235}$U(*n,f*) (*x* = U) or $^{252}$Cf(*s.f*) (*x* = Cf). In addition, for greater statistical precision, the integral spectra obtained in the 0.2 to 0.5 MeV energy range were averaged over three points.

To estimate B($E_n$), use was made of expression (14) and of the fact that the integral prompt fission neutron spectra for $^{252}$Cf(*s.f*) and $^{235}$U(*n,f*) can be represented as Maxwell distributions with parameter *T* equal to 1.42 MeV and 1.314 MeV, respectively [8]:

$$B(E_n{:}T_{\mathrm{U}},T_{\mathrm{Cf}}) = \frac{M(T_{\mathrm{U}},E_n)\cdot\sum_{i=E_n}^{E_n+\Delta E_n} M(T_{\mathrm{Cf}},E_i)}{M(T_{\mathrm{Cf}},E_n)\cdot\sum_{i=E_n}^{E_n+\Delta E_n} M(T_{\mathrm{U}},E_i)}\ ,\quad M(T_M,E) = \frac{2\cdot\sqrt{E}\cdot\exp(-\frac{E}{T_M})}{\sqrt{\pi\cdot T_M^3}}\,, \tag{19}$$

$$D_{BW}(E_n) = \frac{B(E_n{:}T_U,T_{Cf}) - B(E_n{:}T_U+\Delta T_{\mathrm{U}},T_{Cf}+\Delta T_{Cf})}{B(E_n{:}T_U,T_{Cf})}\,, \tag{20}$$

where $M(T_M, E)$ is a Maxwell distribution with an average energy $\langle E\rangle = 3T_M/2$; $\Delta E_n$ is the interval between adjacent nodes on the energy grid on which the integral spectrum was determined; $\Delta T$ is the uncertainty in the data for the parameter $T_M$ for the nuclei being studied (this was taken to be +0.02 MeV and -0.02 MeV for $^{252}$Cf(*s.f*) and $^{235}$U(*n,f*), respectively); $D_{BW}(E_n)$ is the relative precision of the correction $B(E_n)$.

Table 1 shows the values of the corrections applied to the measured ratio of the integral spectra for $^{235}$U(*n,f*) and $^{252}$Cf(*s.f*). Fig. 11 gives a visual representation of the relationship between the corrections to be applied. It can be seen that the ratio of the integral spectra for $^{235}$U(*n,f*) and $^{252}$Cf(*s.f*) obtained by numerically summing the measured fission neutron spectra for the selected angles to the axis of fission depends weakly on the particular features of the experimental set-up being used. Thus, the total correction $F(E_n)$ does not exceed 3% in the 0.2–10 MeV energy range.

Table 1.

**Corrections**

| $E_n$ (MeV) | $f^{\theta}_{res}(E_n)$ | $f^{E}_{res}(E_n)$ | $I(E_n)$ | $B(E_n)$ | $F(E_n)$ |
|---|---|---|---|---|---|
| 16.650 | 1.120 | 0.976 | 0.980 | 1.073 | 1.150 |
| 13.290 | 1.056 | 0.980 | 0.984 | 1.063 | 1.081 |
| 10.860 | 1.019 | 0.982 | 0.985 | 1.052 | 1.036 |
| 9.043 | 1.007 | 0.986 | 0.987 | 1.042 | 1.021 |
| 7.647 | 0.998 | 0.986 | 0.989 | 1.034 | 1.006 |
| 6.552 | 0.996 | 0.989 | 0.990 | 1.028 | 1.002 |
| 5.677 | 0.996 | 0.991 | 0.990 | 1.023 | 1.000 |
| 4.967 | 0.995 | 0.994 | 0.991 | 1.019 | 0.999 |
| 4.383 | 0.994 | 0.996 | 0.992 | 1.016 | 0.998 |
| 3.896 | 0.996 | 0.996 | 0.992 | 1.013 | 0.997 |
| 3.486 | 0.995 | 0.997 | 0.993 | 1.011 | 0.996 |
| 3.137 | 0.994 | 0.998 | 0.992 | 1.010 | 0.993 |
| 2.839 | 0.995 | 0.999 | 0.991 | 1.008 | 0.993 |
| 2.581 | 0.994 | 1.000 | 0.992 | 1.007 | 0.994 |
| 2.357 | 0.995 | 1.000 | 0.992 | 1.006 | 0.994 |
| 2.161 | 0.996 | 1.000 | 0.992 | 1.005 | 0.994 |
| 1.988 | 0.997 | 1.000 | 0.994 | 1.005 | 0.996 |
| 1.835 | 0.997 | 1.000 | 0.994 | 1.005 | 0.996 |
| 1.699 | 0.998 | 1.000 | 0.996 | 1.004 | 0.998 |
| 1.578 | 0.998 | 1.000 | 0.996 | 1.004 | 0.998 |
| 1.469 | 0.998 | 1.000 | 0.997 | 1.003 | 0.998 |
| 1.372 | 0.998 | 1.000 | 0.998 | 1.003 | 0.999 |
| 1.283 | 0.999 | 1.000 | 0.998 | 1.002 | 0.999 |
| 1.203 | 0.998 | 1.000 | 1.000 | 1.002 | 1.000 |
| 1.130 | 0.999 | 1.000 | 0.999 | 1.002 | 1.000 |
| 1.064 | 0.999 | 1.000 | 0.999 | 1.002 | 1.001 |

| $E_n$ (MeV) | $f^{\theta}_{res}(E_n)$ | $f^{E}_{res}(E_n)$ | $I(E_n)$ | $B(E_n)$ | $F(E_n)$ |
|---|---|---|---|---|---|
| 1.003 | 0.999 | 1.000 | 1.000 | 1.002 | 1.001 |
| 0.948 | 0.999 | 1.000 | 0.999 | 1.002 | 0.999 |
| 0.896 | 1.000 | 1.000 | 0.998 | 1.002 | 1.000 |
| 0.849 | 0.999 | 1.000 | 0.998 | 1.002 | 0.999 |
| 0.806 | 0.999 | 1.000 | 0.999 | 1.001 | 0.999 |
| 0.766 | 0.999 | 1.001 | 0.999 | 1.001 | 0.999 |
| 0.728 | 0.999 | 1.000 | 0.998 | 1.001 | 0.998 |
| 0.694 | 0.999 | 1.000 | 0.998 | 1.001 | 0.998 |
| 0.661 | 0.999 | 1.000 | 0.998 | 1.001 | 0.998 |
| 0.631 | 1.000 | 1.000 | 0.997 | 1.001 | 0.998 |
| 0.603 | 0.999 | 1.000 | 0.998 | 1.001 | 0.998 |
| 0.577 | 0.999 | 1.000 | 0.997 | 1.001 | 0.997 |
| 0.553 | 0.999 | 1.000 | 0.998 | 1.001 | 0.998 |
| 0.530 | 0.999 | 1.000 | 0.997 | 1.001 | 0.997 |
| 0.488 | 0.999 | 1.000 | 0.997 | 1.001 | 0.997 |
| 0.434 | 1.000 | 1.000 | 0.997 | 1.002 | 0.999 |
| 0.388 | 0.999 | 1.000 | 0.998 | 1.001 | 0.998 |
| 0.349 | 1.000 | 1.000 | 0.997 | 1.001 | 0.998 |
| 0.316 | 1.000 | 1.000 | 0.998 | 1.001 | 0.999 |
| 0.287 | 0.999 | 1.000 | 0.998 | 1.001 | 0.998 |
| 0.263 | 0.999 | 1.000 | 0.998 | 1.001 | 0.998 |
| 0.241 | 0.999 | 1.000 | 0.998 | 1.001 | 0.998 |
| 0.221 | 0.998 | 1.000 | 0.999 | 1.001 | 0.998 |

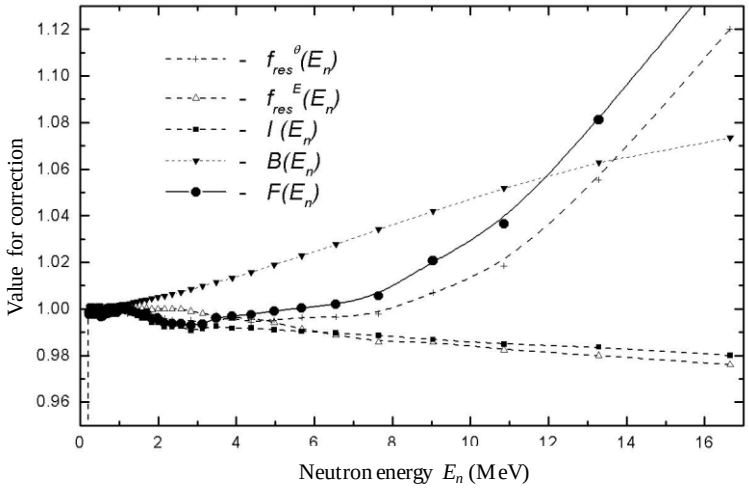


Fig. 11. Values for corrections to be applied to the measured ratio of integral prompt fission neutron spectra for $^{235}$U($n_{th},f$) and $^{252}$Cf(*s.f*) as a function of the energy of the neutron detected.

## Discussion of results

The integral prompt fission neutron spectrum for $^{235}$U(*n,f*), $\Phi_U(E_n)$, was obtained from the measured ratio of the integral prompt fission neutron spectra for $^{235}$U(*n,f*) and $^{252}$Cf(*s.f*), $R(E_n)$, by means of expression (12). The numerical data are given in Table 2. We note that the energy grid onto which the recommended prompt fission neutron spectrum for $^{252}$Cf(*s.f*) was mapped differs from the energy grid used by us for processing the data obtained. For this reason, we used as the standard spectrum, $N_{std}(E_n)$, one that was determined on the actual energy grid and obtained as a linear approximation of the recommended prompt fission neutron spectrum for $^{252}$Cf(*s.f*). The prompt fission neutron spectrum for $^{252}$Cf(*s.f*) determined in this manner is also shown in Table 2.

Table 2.

**Prompt fission neutron spectrum for $^{235}$U(*n,f*)**

| $E_n$ (MeV) | $R(E_n)$ | $D_R$ (% × $10^{-2}$) | $D_U$ (% × $10^{-2}$) | $D_{Cf}$ (% × $10^{-2}$) | $D_{Bckg}$ (% × $10^{-2}$) | $D_W$ (% × $10^{-2}$) | $D_{En}$ (% × $10^{-2}$) | $N_{Std}(En)$ (1/MeV × $10^4$) | $D_{Std}$ (% × $10^{-2}$) | $\Phi_U(E_n)$ (neutrons/MeV × $10^4$) | $D_\Phi$ (% × $10^{-2}$) |
|---|---|---|---|---|---|---|---|---|---|---|---|
| 16.650 | 0.1577 | 0.469 | 0.367 | 0.142 | 0.231 | 0.027 | 0.376 | 0.1812 | 0.156 | 0.1074 | 0.494 |
| 13.290 | 0.2961 | 0.259 | 0.143 | 0.107 | 0.156 | 0.023 | 0.284 | 1.759 | 0.045 | 1.958 | 0.263 |
| 10.860 | 0.3880 | 0.167 | 0.068 | 0.076 | 0.059 | 0.019 | 0.221 | 9.103 | 0.029 | 13.3 | 0.170 |
| 9.043 | 0.4299 | 0.127 | 0.038 | 0.062 | 0.027 | 0.016 | 0.177 | 30.7 | 0.022 | 49.6 | 0.129 |
| 7.647 | 0.4778 | 0.098 | 0.031 | 0.041 | 0.015 | 0.013 | 0.143 | 77.9 | 0.019 | 139.9 | 0.100 |
| 6.552 | 0.5403 | 0.079 | 0.024 | 0.032 | 0.010 | 0.010 | 0.118 | 160.8 | 0.016 | 326.6 | 0.081 |
| 5.677 | 0.5651 | 0.067 | 0.016 | 0.031 | 0.007 | 0.009 | 0.098 | 283.6 | 0.015 | 602.4 | 0.068 |
| 4.967 | 0.5912 | 0.054 | 0.015 | 0.021 | 0.004 | 0.007 | 0.082 | 444.5 | 0.014 | 987.8 | 0.056 |
| 4.383 | 0.6169 | 0.046 | 0.013 | 0.019 | 0.003 | 0.006 | 0.069 | 640.0 | 0.013 | 1484.2 | 0.048 |
| 3.896 | 0.6266 | 0.039 | 0.011 | 0.017 | 0.002 | 0.005 | 0.058 | 859.1 | 0.012 | 2023.6 | 0.041 |
| 3.486 | 0.6449 | 0.033 | 0.010 | 0.014 | 0.002 | 0.004 | 0.049 | 1092 | 0.012 | 2647.1 | 0.035 |
| 3.137 | 0.6494 | 0.031 | 0.009 | 0.016 | 0.001 | 0.004 | 0.042 | 1331 | 0.012 | 3249.0 | 0.033 |
| 2.839 | 0.6437 | 0.026 | 0.008 | 0.015 | 0.001 | 0.003 | 0.035 | 1564 | 0.012 | 3784.3 | 0.029 |
| 2.581 | 0.6552 | 0.023 | 0.007 | 0.014 | 0.001 | 0.003 | 0.030 | 1785 | 0.012 | 4396.4 | 0.026 |
| 2.357 | 0.6784 | 0.022 | 0.007 | 0.015 | 0.001 | 0.002 | 0.025 | 1994 | 0.011 | 5084.7 | 0.024 |
| 2.161 | 0.6632 | 0.019 | 0.008 | 0.012 | 0.001 | 0.002 | 0.021 | 2187 | 0.011 | 5452.3 | 0.021 |
| 1.988 | 0.6782 | 0.018 | 0.008 | 0.013 | 0.001 | 0.002 | 0.017 | 2365 | 0.012 | 6028.9 | 0.022 |
| 1.835 | 0.6761 | 0.017 | 0.008 | 0.012 | 0.001 | 0.002 | 0.014 | 2524 | 0.012 | 6415.1 | 0.020 |
| 1.699 | 0.6744 | 0.015 | 0.007 | 0.011 | 0.001 | 0.002 | 0.011 | 2671 | 0.013 | 6770.6 | 0.020 |
| 1.578 | 0.6616 | 0.018 | 0.008 | 0.015 | 0.001 | 0.001 | 0.009 | 2792 | 0.012 | 6943.5 | 0.021 |
| 1.469 | 0.6646 | 0.017 | 0.008 | 0.015 | 0.001 | 0.001 | 0.007 | 2900 | 0.012 | 7245.3 | 0.021 |
| 1.372 | 0.6765 | 0.019 | 0.007 | 0.017 | 0.001 | 0.001 | 0.005 | 2995 | 0.012 | 7615.8 | 0.022 |
| 1.283 | 0.6735 | 0.014 | 0.009 | 0.010 | 0.001 | 0.001 | 0.003 | 3075 | 0.012 | 7784.4 | 0.018 |
| 1.203 | 0.6686 | 0.016 | 0.008 | 0.014 | 0.001 | 0.001 | 0.002 | 3147 | 0.012 | 7909.7 | 0.020 |
| 1.130 | 0.6817 | 0.014 | 0.009 | 0.011 | 0.001 | 0.001 | 0.001 | 3199 | 0.012 | 8197.6 | 0.019 |
| 1.064 | 0.6763 | 0.019 | 0.009 | 0.017 | 0.001 | 0.001 | 0.001 | 3243 | 0.013 | 8244.2 | 0.023 |
| 1.003 | 0.6746 | 0.021 | 0.009 | 0.019 | 0.001 | 0.001 | 0.001 | 3283 | 0.016 | 8325.0 | 0.026 |
| 0.948 | 0.6776 | 0.017 | 0.009 | 0.014 | 0.001 | 0.001 | 0.001 | 3311 | 0.017 | 8432.8 | 0.024 |
| 0.896 | 0.6668 | 0.024 | 0.011 | 0.021 | 0.001 | 0.001 | 0.001 | 3333 | 0.018 | 8354.2 | 0.030 |
| 0.849 | 0.6681 | 0.019 | 0.010 | 0.016 | 0.001 | 0.001 | 0.001 | 3352 | 0.018 | 8418.5 | 0.026 |
| 0.806 | 0.6648 | 0.024 | 0.011 | 0.021 | 0.001 | 0.001 | 0.001 | 3360 | 0.018 | 8396.8 | 0.030 |
| 0.766 | 0.6756 | 0.025 | 0.011 | 0.022 | 0.001 | 0.001 | 0.002 | 3360 | 0.018 | 8533.3 | 0.031 |
| 0.728 | 0.6717 | 0.021 | 0.013 | 0.017 | 0.001 | 0.001 | 0.003 | 3360 | 0.019 | 8483.7 | 0.029 |
| 0.694 | 0.6623 | 0.025 | 0.011 | 0.022 | 0.001 | 0.000 | 0.004 | 3360 | 0.018 | 8365.1 | 0.031 |
| 0.661 | 0.6720 | 0.026 | 0.013 | 0.022 | 0.001 | 0.000 | 0.006 | 3353 | 0.017 | 8469.8 | 0.031 |
| 0.631 | 0.6597 | 0.023 | 0.013 | 0.019 | 0.001 | 0.000 | 0.008 | 3341 | 0.016 | 8285.0 | 0.028 |
| 0.603 | 0.6660 | 0.028 | 0.015 | 0.023 | 0.001 | 0.000 | 0.010 | 3329 | 0.017 | 8335.0 | 0.033 |
| 0.577 | 0.6782 | 0.029 | 0.014 | 0.024 | 0.002 | 0.000 | 0.012 | 3318 | 0.018 | 8458.3 | 0.034 |
| 0.553 | 0.6602 | 0.030 | 0.015 | 0.025 | 0.002 | 0.000 | 0.015 | 3298 | 0.018 | 8184.7 | 0.035 |
| 0.530 | 0.6666 | 0.032 | 0.015 | 0.027 | 0.002 | 0.000 | 0.017 | 3280 | 0.018 | 8218.7 | 0.037 |
| 0.488 | 0.6853 | 0.022 | 0.010 | 0.015 | 0.002 | 0.000 | 0.023 | 3229 | 0.017 | 8318.2 | 0.028 |
| 0.434 | 0.6671 | 0.027 | 0.010 | 0.016 | 0.002 | 0.001 | 0.033 | 3164 | 0.017 | 7933.9 | 0.032 |
| 0.388 | 0.6411 | 0.035 | 0.011 | 0.022 | 0.002 | 0.000 | 0.044 | 3076 | 0.017 | 7423.1 | 0.039 |
| 0.349 | 0.7089 | 0.044 | 0.014 | 0.027 | 0.003 | 0.001 | 0.055 | 2998 | 0.017 | 7988.8 | 0.047 |
| 0.316 | 0.6603 | 0.047 | 0.015 | 0.021 | 0.003 | 0.000 | 0.067 | 2921 | 0.017 | 7249.8 | 0.050 |
| 0.287 | 0.6681 | 0.057 | 0.019 | 0.029 | 0.003 | 0.000 | 0.079 | 2840 | 0.018 | 7132.0 | 0.060 |
| 0.263 | 0.6328 | 0.068 | 0.022 | 0.037 | 0.003 | 0.000 | 0.090 | 2755 | 0.018 | 6553.5 | 0.070 |
| 0.241 | 0.6919 | 0.077 | 0.028 | 0.042 | 0.007 | 0.000 | 0.101 | 2675 | 0.019 | 6957.0 | 0.080 |
| 0.221 | 0.6824 | 0.097 | 0.036 | 0.059 | 0.029 | 0.000 | 0.113 | 2598 | 0.021 | 6664.2 | 0.099 |

The total relative error for the integral spectrum obtained, $D_\Phi$, was calculated assuming that all the errors considered were independent and that the systematic errors have an orthogonal distribution:

$$D_{\Phi}^2 = D_R^2 + D_{Std}^2 = D_{\mathrm{U}}^2 + D_{\mathrm{Cf}}^2 + \frac{\left(D_{Bckg}^2 + D_{BW}^2 + D_{En}^2\right)}{3} + D_{Std}^2, \quad (21)$$

where $D_{\mathrm{U}}$ and $D_{\mathrm{Cf}}$ are the relative measurement error for the integral prompt fission neutron spectrum obtained by means of expression (17) for $^{235}$U(*n,f*) and $^{252}$Cf(*s.f*), respectively; $D_{Std}$ is the relative precision of the standard $N_{\mathrm{Std}}(E_n)$ [3]; $D_{Bckg}$ is the relative maximum uncertainty of the ratio $R(E_n)$ due to systematic errors in determining the neutron detector background; $D_{En}$ is the relative maximum uncertainty of the ratio $R(_{En})$ resulting directly from the fact that the length of the neutron detector is comparable to the length of the flight path: $h/D \approx 8\%$.

As noted above, linear approximation was used to estimate the background component which cannot be determined experimentally. To estimate the effect of this on the final result, the processing of the experimental data $R^*(E_n)$ was performed in two versions, using a different set of approximation parameters. In both cases, the residual background component was represented as a constant and was defined as the average value for the left edge (number of events before the peak of fragment-γ-quantum coincidences) and the right edge (number of events in channels larger than the discrimination threshold in the neutron channels) of the time-of-flight spectra for the first and second processing version, respectively. For the corresponding systematic error, we took the energy dependence:

$$D_{Bckg}(E_n) = max\left(\frac{|(R^*(E_n) - R(E_n)|}{R(E_n)}\right). \quad (22)$$

To estimate the maximum uncertainty, $D_{En}$, the ratio of the integral prompt fission neutron spectra for $^{235}$U(*n,f*) and $^{252}$Cf(*s.f*), $R^+(E_n)$ and $R^-(E_n)$, were calculated for two flight distances, respectively:

$$D = d + h/2 + \delta d \quad \text{and} \quad D = d - h/2 - \delta d. \quad (23)$$

The ratios $R^+(E_n)$ and $R^-(E_n)$ obtained in this way are shown in Fig. 12. Next, the corresponding systematic error for the ratio $R(E_n)$ was determined by means of expression (24):

$$D(E_n) = \frac{|R^+(E_n) - R(E_n)| + |R^-(E_n) - R(E_n)|}{2 \cdot R(E_n)}. \quad (24)$$

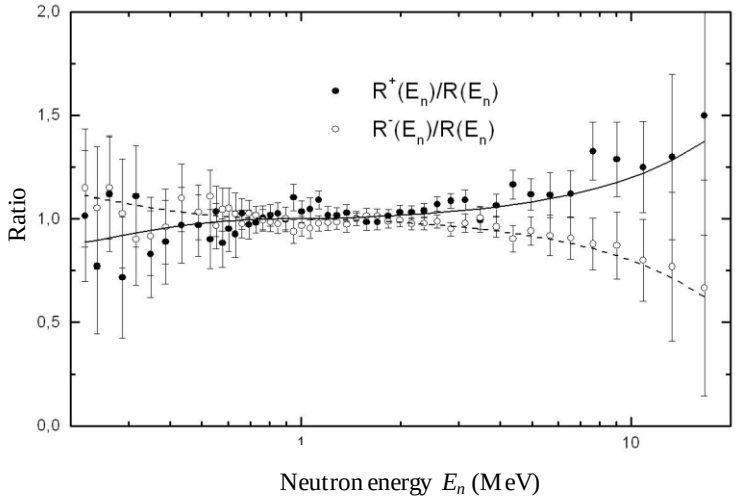


Fig. 12. Ratio of the integral prompt fission neutron spectra for $^{235}$U($n_{th}$, *f*) and $^{252}$Cf(*s.f*) obtained for two flight paths defined as the distance from the fissioning target to the front and rear surface of the stilbene crystals used.

Fig. 13 shows the prompt fission neutron spectrum obtained for $^{235}$U(*n,f*) in terms of a ratio to the Maxwell distribution with parameters $\nu_U$ = 2.421 (ENDF/B-VII) and $T_M$ = 1.314 MeV [8]

$$\mu(E_n) = \frac{R(E_n)\cdot N_{Std}(E_n)\cdot \nu_{\mathrm{Cf}}}{M(1.314,E_n)\cdot \nu_{\mathrm{U}})} = \frac{\Phi_{\mathrm{U}}(E_n)}{M(1.314,E_n)\cdot \nu_{\mathrm{U}}}. \quad (25)$$

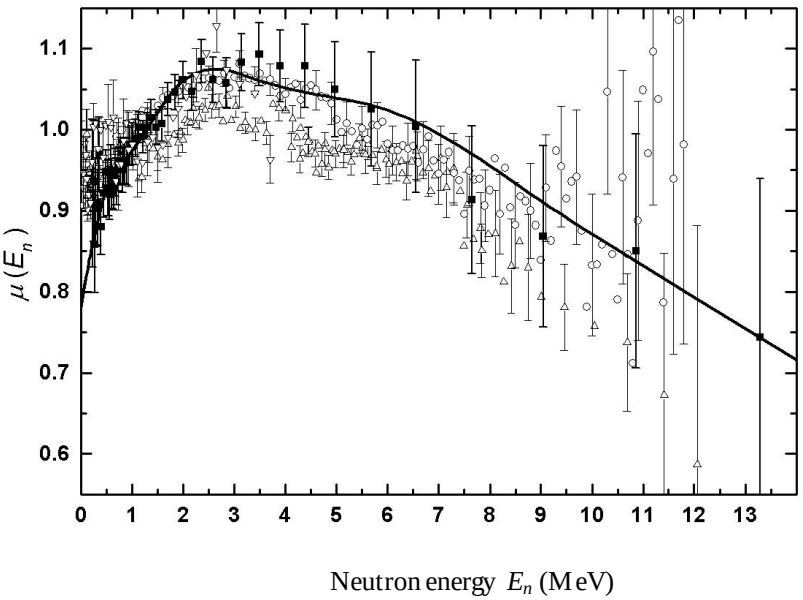


Fig. 13. Ratio of the integral prompt fission neutron spectrum for $^{235}$U($n_{th}$, *f*) to the Maxwell distribution (19) with $T_M$ = 1.314 MeV: ■ – this paper; ○ – [10]; ▲ – [8]; ∇ - [9]; ▬ estimate from ENDF/B-VII.

For comparison, the results of other work [8–10] and an estimate from ENDF/B-VII [3] of the shape of the fission neutron spectrum for thermal-neutron induced fission of $^{235}$U(*n,f*) are also shown. All the experimental spectra shown were obtained by the time-of-flight method from the measured ratios of the spectra for $^{235}$U(*n,f*) and $^{252}$Cf(*s.f*) using expression (25). In [8], different neutron detectors were used according to the neutron energy range being studied:

1) 0.08–0.9 MeV – anthracene crystal with FEU-71 photomultiplier (flight distance 51 cm);
2) 1–8 MeV – stilbene crystal with FEU-63 photomultiplier (flight distance 231.3 cm);
3) 4–12 MeV – plastic with FEU-63 photomultiplier (flight distance 611 cm).

The neutron detector used in [9] to study the spectra in the 0.03–4 MeV energy range consisted of NE-912 lithium glass with a FEU 30 photomultiplier (flight distance 30 cm), and in [10] a SCIONIX LS301 liquid scintillator (equivalent to NE-213) with XP4312 photomultiplier was used and the flight distance was 300 cm.

This presentation makes it possible to assess the degree of reliability of the data obtained and determine the potential systematic errors associated with this measurement method. Since the absolute precision in determining the total number of fission events $N_f$ (normalization precision) in the experiments depicted in Fig. 13 is approx. 1–2%, in order to exclude this uncertainty from the systematic error for the method an additional normalization was performed on the spectra obtained (Fig. 14):

$$\mu'(E_n) = K_N \cdot \mu(E_n)\,, \quad K_N = \frac{\nu_U}{\nu_{fit}}, \tag{26}$$

where $K_N$ and $\nu_{fit}$ are the normalization coefficient and the average total number of neutrons per fission for $^{235}$U(*n,f*) obtained from a description of the experimental data using a smooth function, respectively. It is well known [11] that for model-free description of prompt fission neutron spectra, besides a Maxwell distribution, as in (19), a Watt distribution can be used:

$$W(T_W, E_W, E_n) = \nu_{fit} \cdot (\pi \cdot E_W \cdot T_W)^{-\frac{1}{2}} \cdot \exp\left(-\frac{E_W + E_n}{T_W}\right) \cdot \sinh\left(\frac{2\cdot\sqrt{E_W + E_n}}{T_W}\right), \tag{27}$$

with average energy

$$\langle E_n \rangle = E_{W+} \frac{3\cdot T_W}{2}, \tag{28}$$

which yields a better description of the experimental data in the hard part of the spectrum. Hence, the neutron spectra shown in Fig. 13 were interpolated in the 1–10 MeV energy range using expression (27). The results describing each experimental prompt fission neutron spectrum for $^{235}$U(*n,f*) in this way are shown in Table 3. We note that the data in [8], which were obtained using two different detectors in the 4–8 MeV energy range, coincide within the limits of experimental error and thereafter were treated as a single set of data (Fig. 13). This table also shows the results of describing the experimental spectra using a Maxwell distribution. The values obtained for the normalization coefficient $K_N$ for the Watt distribution fall within the absolute precision limits for the experimental data, whereas for the Maxwell distribution the deviation from 1 of the $K_N$ values obtained exceeds the experimental precision of normalization. This was a further argument in favour of choosing the Watt distribution as the interpolation function for determining the normalization coefficient $K_N$ in expression (26).

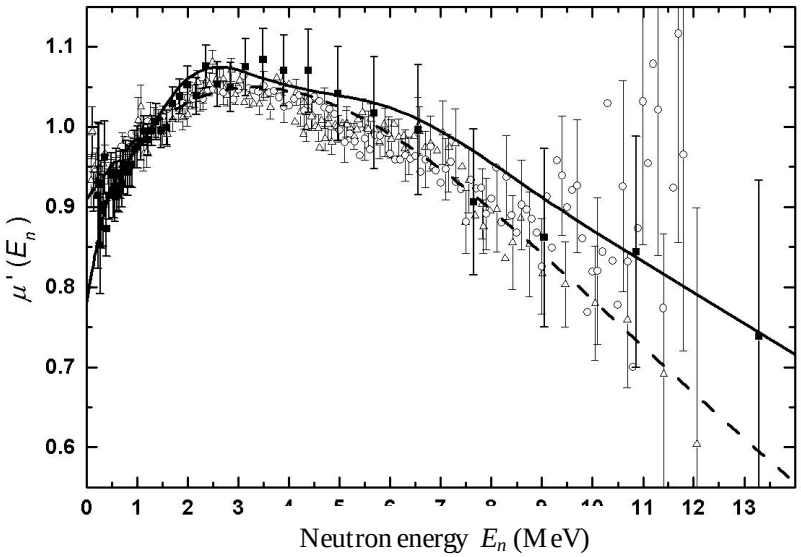


Fig. 14. Ratio of the integral prompt fission neutron spectrum for $^{235}$U($n_{th}$, *f*) after additional normalization to the Maxwell distribution in (19) with $T_M$ = 1.314 MeV: ■ – this paper; ○ – [10]; ▲ – [8]; ▬ estimate from ENDF/B-VII; – – – Watt distribution (27) based on data from [8].

From Fig. 14 we see that there is agreement in the shape of the fission neutron spectrum for $^{235}$U(*n,f*) within the limits of error for the experimental data in the 1–10 MeV energy range (more

than 80% of the total number of neutrons). The experimental data shown in Fig. 14 can also be described, within the limits of experimental error, using the estimate from ENDF/B-VII arrived at under the assumption of isotropic emission of prompt fission neutrons from fully accelerated fission fragments after disintegration of the nucleus. In this case the value of the normalization coefficient $K_N$ for the data in [8] exceeds the experimental uncertainty of normalization and comes to approx. 1.045, respectively.

At low energies on the prompt fission neutron spectrum (0.1–1 MeV) the uncertainty for the experimental data is somewhat greater (Fig. 15). This is probably due to particularities in accounting for the neutron detector background. The situation is further complicated by the fact that when analysing data from experimental work [8, 9] it is not possible to exclude the uncertainty due to imprecision in the normalization, as was done for neutron energies over 1 MeV. For this reason, experimentally determining the shape of the prompt fission neutron spectrum at low energies requires experimental data obtained using the time-of-flight method by different groups of experimenters using different neutron and fission fragment detectors.

Table 3.

**Watt distribution parameters. The errors given are the mean square deviation of the experimental data points from the distribution used**

| Watt distribution parameters (27) | | | | | |
|---|---|---|---|---|---|
| Ref. | $T_W$ (MeV) | $E_W$ (MeV) | Average energy $<E_n>$ (MeV) | $\nu_{fit}$ | Normalization coefficient $K_N$ |
| This paper | 0.954 ± 0.033 | 0.592 ± 0.041 | 2.023 ± 0.012 | 2.440 ± 0.014 | 0.992 |
| [8] | 0.983 ± 0.031 | 0.521 ± 0.041 | 1.995 ± 0.011 | 2.353 ± 0.011 | 1.029 |
| [10] | 0.968 ± 0.006 | 0.534 ± 0.008 | 1.985 ± 0.003 | 2.461 ± 0.002 | 0.984 |
| Maxwell distribution parameters (19) | | | | | |
| | $T_M$ (MeV) | Average energy $<E_n>$ (MeV) | | $\nu_{fit}$ | $K_N$ |
| This paper | 1.390 ± 0.009 | 2.089 ± 0.014 | | 2.509± 0.010 | 0.965 |
| [8] | 1.353 ± 0.006 | 2.030 ± 0.009 | | 2.404 ± 0.006 | 1.007 |
| [10] | 1.339 ± 0.003 | 2.009 ± 0.004 | | 2.513 ± 0.004 | 0.963 |

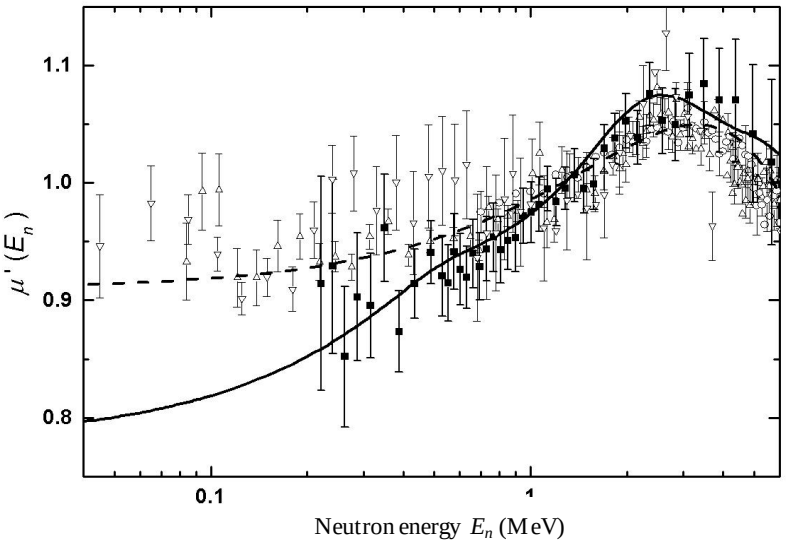


Fig. 15. Ratio of the integral prompt fission neutron spectrum for $^{235}U(n_{th}, f)$ after additional normalization to the Maxwell distribution in (19) with $T_M$ = 1.314 MeV: ■ – this paper; ○ – [10]; ▲ – [8]; ∇ - [9]; ▬ estimate from ENDF/B-VII; – – - Watt distribution (27) based on data from [8].

Thus, the best description of the experimental data is achieved by using the Watt distribution. Some of the difference in shape between the evaluated prompt fission neutron spectrum (ENDF/B-VII) and the experimental spectra could be due to experimental difficulties in determining the spectrum and to the limitations of the model used. The statistical model for the evaluation of the prompt fission neutron spectrum (ENDF/B-VII) should probably take into account the anisotropy of neutron emission due to the angular momentum of the fragments and the possibility that there are neutrons being emitted from non-fully accelerated fragments and at the initial stage of the fission process ('scission neutrons') [12]. It is worth noting that, unlike the work presented in Figs 13–15, in the present paper the integral prompt fission neutron spectrum was determined by numerical integration of the partial prompt fission neutron spectra obtained for fixed angles to the axis of fission. Given that agreement is observed, within the limits of experimental error, in the data obtained using different methods, one may conclude that scission neutrons make up a rather small part of the prompt fission neutron spectrum.

The authors consider it their pleasant duty to express their thanks to G.A. Petrov for posing the problem and for fruitful discussions of the work and the results obtained. The authors greatly appreciate the contributions to this work made by A.M. Gagarski, Yu.S. Pleva, G.V. Valsky, V.I. Petrova, T.A. Zavarukhina and V.E. Sokolov, who took part in preparing and performing the experiment.

**References**

1. Vorobyev A.S., Shcherbakov O.A., Pleva Yu.S., *et.al*., Nucl. Instr. and Meth. **A598**, 795 (2009).
2. Vorobyev A.S., Shcherbakov O.A., Pleva Yu.S., *et.al*., in: A.M. Sukhovoj (Ed.), XVII$^{th}$ International Seminar on Interaction of Neutrons with Nuclei "Neutron Spectroscopy, Nuclear Structure, Related Topics", ISINN-17, Dubna, May 27–29, 2009, JINR, Dubna, E3-2010-36, 2010, p. 60.
3. Reich C.W., Mannhart W., England T., ENDF/B-VII.
4. Seregina E.A., Dyachenko P.P // VANT, Ser. Yadernye konstanty, 1985, No. 1, p. 58.
5. Bowman H.R., Thompson S.G., Milton J.C.D., and Swiatecki W.J., Phys. Rev. **126**, 2120 (1962).
6. Poenitz W.P. and Tamura T. in "Nuclear Data for Science and Technology", Bockhoff K.H. (ed.), 465–472, 1983.
7. Seregina E.A., Dyachenko P.P. // Yadernaya Fizika, 1985, vol. 42, No. 6(12), p. 1337.
8. Starostov B.I., Nefedov V.N., Boytsov A.A. // Proceedings of the Sixth All-Union Conference on Neutron Physics, Kiev, 2–6 October 1983, vol. 2, p. 285 (Moscow, 1984); Starostov B.I., Nefedov V.N., Boytsov A.A. // VANT, Ser. Yadernye konstanty, 1985, No. 3, p. 16, EXFOR 40871011, 40871012, 40872007.
9. Lajtai, J. Kecskemeti, J. Safar, *et. al.*, IAEA-TECDOC-335, p. 312 (1985), EXFOR 3070403.
10. Kornilov N., Hambsch F.-J., Fabry I., *et. al.*, Nucl. Sci. and Eng. **165**, 117 (2010).
11. Terrell J., Phys. Rev. **113**, 527 (1959).
12. Vorobyev A.S., Shcherbakov O.A., Gagarski A.M., *et.al.*, EPJ Web of Conference **8**, 03004 (2010). DOI: 10.1051/epjconf/20100803004.

**Nuclear Data Section**
International Atomic Energy Agency
Vienna International Centre, P.O. Box 100
A-1400 Vienna
Austria

e-mail: services@iaeand.iaea.org
fax: (43-1) 26007
telephone: (43-1) 2600-21710
Web: http://www-nds.iaea.org/